# Label-free DIA-NN enabled RIME (DIANNeR) reveals glucocorticoid receptor interaction networks in breast, bladder, and blood across normal untransformed cells, cancer cell lines, and PDXs

Weiye Zhao[1], Susanna F Rose[1], Thomas F Grimes[1], Jack Stenning[1], Chris Taylor[2], Chloë Baldreki[2], Iain Goulding[4], Ros Duke[1], Simon C Baker[1], Marcela Montes de Oca[1,3], Aparna Sinha[1], Jenny Hinley[1], James M Fox[1], Paul M Kaye[3], Jennifer J Gomm[4], Louise J Jones[4], Elisabetta Marangoni[5], Bruno M Simões[6], Robert B Clarke[6], Jennifer Southgate[1], Katherine S Bridge[1], Adam Dowle[2], Andrew N Holding[1*]

1. Department of Biology and York Biomedical Research Institute, University of York, York YO10 5DD, UK
2. Metabolomics and Proteomics, Biosciences Technology Facility, Department of Biology, University of York, York YO10 5DD, UK
3. Hull York Medical School and York Biomedical Research Institute, University of York, York YO10 5DD, UK
4. Breast Cancer Now Biobank, Centre for Tumour Biology, Barts Cancer Institute, John Vane Science Centre, Queen Mary University of London, London EC1M 6AU, UK
5. Translational Research Department, Institut Curie, 26 rue d'Ulm, 75005 Paris, France
6. Manchester Breast Centre, Division of Cancer Sciences, Faculty of Biology, Medicine and Health, University of Manchester, Manchester, UK

*To whom correspondence should be addressed. Email: andrew.holding@york.ac.uk.

# Abstract

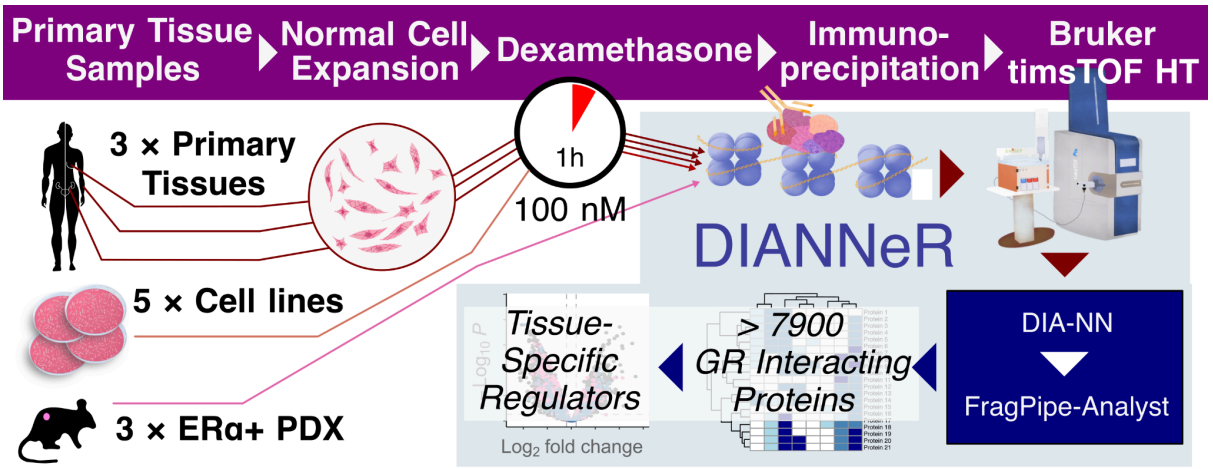



The glucocorticoid receptor (GR) coordinates diverse transcriptional responses to glucocorticoids, regulating metabolism, inflammation, homeostasis, and development. Although GR is expressed in nearly every cell type, its activity is tissue-specific and shaped by context-dependent protein interactions. To enable comprehensive, quantitative profiling of GR interactomes across tissue types and cell states, we developed DIANNeR: a label-free proteomic pipeline combining immunoprecipitation with data-independent acquisition mass spectrometry (DIA-MS) and the DIA-NN software.

DIANNeR provides a 2-fold increase in quantification of specific protein–protein interactions over DDA-RIME, without requiring isotopic labelling. Applied to GR, DIANNeR revealed distinct context-dependent interaction networks. We observed loss of a HOXA5–GR interaction during the transition from breast epithelium to cancer lines and patient-derived xenografts (PDXs), and a $CD4^+$ T cell-specific GR interaction with FOXP3 and BCL11B, not detected in epithelial or Jurkat cells. Conversely, the SWI/SNF complex subunit SMARCD3 was consistently enriched in GR interactomes from normal human breast and urothelial cells but absent in $CD4^+$ T cells, suggesting lineage-specific roles and the potential for selective modulation of GR activity in different contexts.

Our findings establish DIANNeR as a robust, scalable platform for resolving tissue-specific transcription factor interactomes, and reveal features of GR signalling with implications for cancer biology and immunology.

**200/200 words**


# Introduction

The glucocorticoid receptor (GR or NR3C1) is expressed ubiquitously in cells, yet the response to glucocorticoid steroids varies widely across different tissues (1, 2). Cortisol, the natural ligand of the GR, is a glucocorticoid steroid hormone produced by the adrenal gland

that plays a central role in organismal homeostasis within a diverse set of physiological functions (3, 4). Synthetic analogues of cortisol, such as dexamethasone, hydrocortisone and prednisolone, are some of the most widely used therapeutic compounds due to their low cost, effectiveness, and broad availability (3). The physiological and therapeutic importance of these compounds underscores the need to better understand how the GR regulates such diverse signalling pathways, especially considering how a single compound can enact profoundly different responses (2, 3). In T lymphocytes, for example, glucocorticoids can induce apoptosis during development and maturation (5), whereas in mammary tissue, glucocorticoids prevent breast epithelial cell apoptosis, which protects the mammary gland from involution during lactation (6).

Glucocorticoids are primarily used in clinical settings as an anti-inflammatory medication (7). Synthetic alternatives with higher potency are also used as therapeutics to treat lymphoid malignancies (due to their lymphocytic toxicity) (8–10), and manage the side effects of anti-cancer therapies and cancer-related symptoms (7, 11). In this context, their roles are diverse: while glucocorticoids reduce the proliferation of estrogen receptor (ER) positive breast cancer cells (12, 13), the same treatments can induce tumour cell migration and metastasis of triple-negative breast cancer (TNBC) and worsened survival (14–16). The contrasting effects of glucocorticoids in breast cancer treatment highlight the need for a deep mechanistic understanding of tissue-specific glucocorticoid responses (12). Especially, with their essential use to manage symptoms of cancer, there is clinical imperative to prevent glucocorticoid treatment-induced metastasis in TNBC (7, 17).

Mechanistically, inactive GR localised to the cytoplasm is activated when it binds an available ligand. The protein then undergoes a conformational change, leading to dissociation from heat shock proteins and molecular chaperones, before being imported through cytoskeletal fibres into the nucleus (18). The activated GR acts as a transcription factor (TF) to regulate the expression of GR target genes (19, 20). Evidence supports the model that GR orchestrates target gene expression by recruiting a diverse range of coregulators, including other TFs (19–22), scaffold proteins, chromatin remodellers and histone modifiers dictating tissue-specific glucocorticoid responses (20, 23). Notably, functional studies of single GR coregulators in different tissue types have shown distinct roles in glucocorticoid-regulated gene expression and pathways. For example, GR coactivator EHMT2 regulates genes linked with cell migration in A549 lung cancer cells (24), while in the Nalm6 B-ALL cell line model, the same protein influences cell viability (25). Equally, NCOA2 (GRIP1) is a common coactivator for GR and other nuclear receptors in solid tissues (23), but facilitates the GR-governed repression of proinflammatory genes in macrophages (26), further illustrating the complex and context-dependent roles of GR coregulators.

Recent advances in proteomic technologies for studying chromatin-bound complexes by immunoprecipitation (IP) coupled with Liquid Chromatography-Mass Spectrometry (LC-MS) (including Rapid immunoprecipitation mass spectrometry of endogenous proteins (RIME) (27), qPLEX-RIME (28), and ChIP-MS (29)) have enabled the comprehensive profiling of nuclear TF interactomes (29). These methods have revealed novel GR coregulators in specific

tissues and cell types (30–33), but are typically applied to a single biological context. Consequently, the majority of GR interactome data is fragmented across different organisms, experimental platforms, and methodologies, limiting direct quantitative comparison between tissues.

To address this challenge, we present DIA-NN enabled RIME (DIANNeR). Our method enables high-throughput, label-free, cross-tissue analysis of chromatin interactomes from normal human cells in finite culture, immortalised cell lines and PDXs **(Table S1)**. While developed and benchmarked against data-dependent acquisition (DDA) based RIME, and using the glucocorticoid receptor (GR) as a model, DIANNeR is broadly applicable to other nuclear receptors and TFs **(Figure 1A)**. Our approach integrates the advantages of label-free data-independent acquisition (DIA) (34), which exceeds DDA in terms of speed of acquisition and depth of quantitative coverage (34–36). Recently, DIA has been enhanced further with technological advancements in mass spectrometry (MS) technology, e.g. ion mobility separation (IMS), and instruments including the Bruker timsTOF (37) and the Thermo Orbitrap Astral (38). However, a challenge of DIA analysis is spectral complexity, with individual fragmentation spectra containing potentially dozens of co-eluting peptides. Traditional library-based DIA approaches require spectral libraries that are created from preceding DDA acquisitions (35). This limitation presents a challenge as library generation can require further fractionation and longer run lengths than the DIA acquisitions themselves. Although DIA can be argued to have originated in library-free workflows with $MS^E$ acquisition (39), it is only more recently, with software packages such as DIA-NN (40) and Spectronaut (41), that high-depth and library-free DIA data analysis has become tractable. Thus, through systematic optimisation of antibody selection, protocol scale, acquisition mode, and IMS, followed by integration with the DIA-NN and FragPipe-Analyst (42) pipelines, and benchmarking against DDA-RIME, we establish DIANNeR as a robust, high-throughput, and reproducible approach for profiling GR chromatin interactomes across tissues and models. Demonstrating the value of DIANNeR for studying the GR interactome, we applied our method to a panel of human models spanning normal cells, non-tumourigenic immortalised lines, established cancer cell lines, and patient-derived xenografts (PDXs), across epithelial, lymphoid, and urothelial lineages **(Table S1)**, and identified lineage- and status-specific changes in GR-associated protein networks.

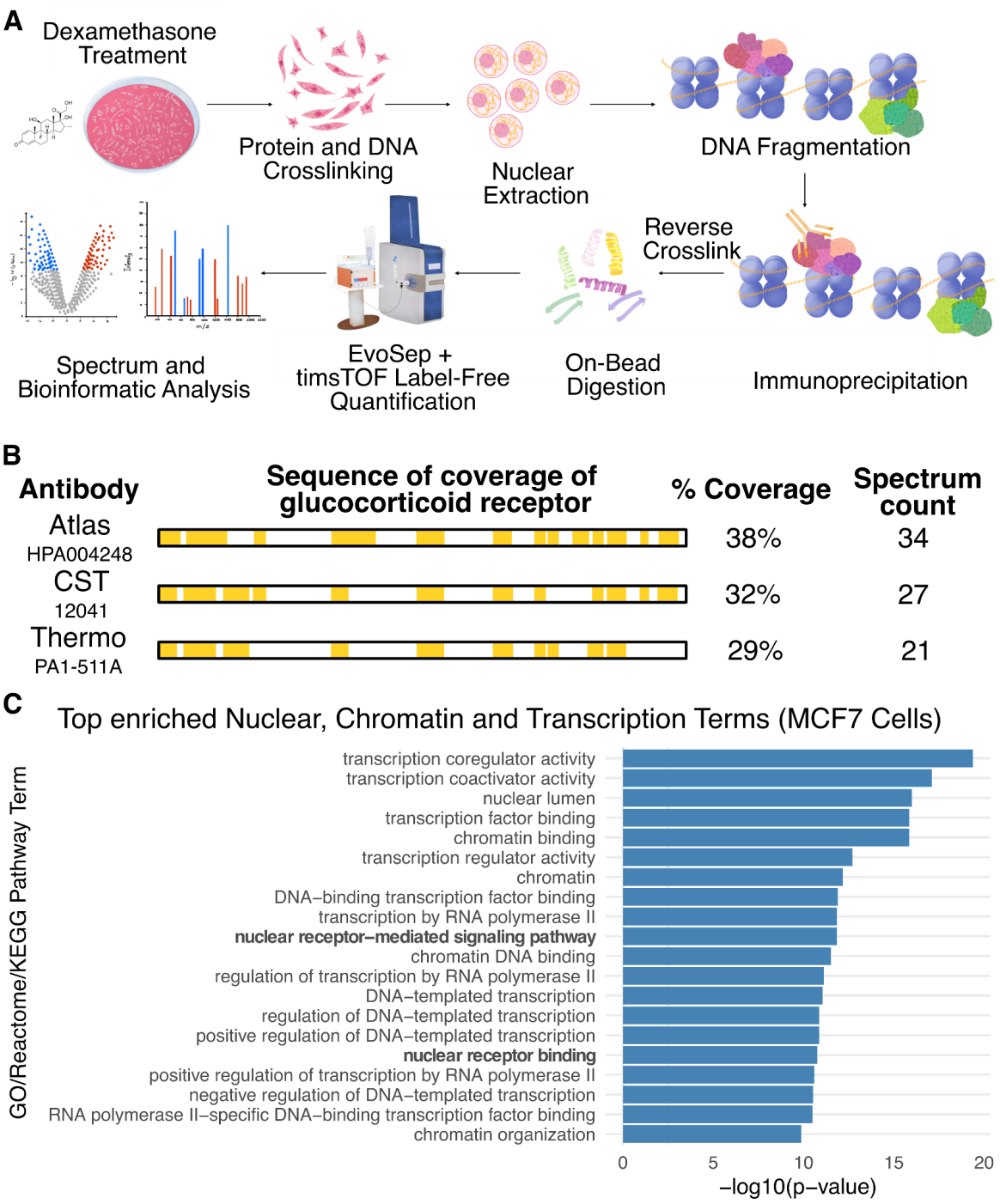


**Figure 1 (A)** Schematic overview of the DIANNeR workflow. **(B)** The peptide spectrum count and coverage on GR resulting from DDA-MS analysis with candidate GR antibodies. **(C)** Top 20 enriched nuclear, chromatin and transcription terms from analysis of GR interactors detected using the Atlas (HPA004248) antibody and DDA-RIME.

# Materials & Methods

## Cell culture

All cell types were cultured at 37°C in a humidified atmosphere containing 5% carbon dioxide in air. MCF7, MCF10A, MDA-MB-231, KMBC2 and Jurkat cell lines were routinely tested and confirmed negative for Mycoplasma spp. infection using Mycostrip (rep-mys-20, Invivogen). The authenticity of these five established human cell lines was confirmed by short tandem repeat (STR) profiling. Primary human breast epithelial cells were obtained from the Breast Cancer Now Biobank (REC 21/EE/0072). Breast tissue from cosmetic reduction mammoplasty was digested using a two-step enzymatic process, collagenase and hyaluronidase treatment, followed by sedimentation and subsequent trypsinization to obtain a single-cell suspension. Breast epithelial cells were isolated using Fluorescence Activated Cell Sorting (FACS) using anti-EPCAM PE (347198, BD biosciences). Sorted cells were then cultured on collagen-coated plates and expanded with up to 2 passages to reach the number of cells required. Full details are provided in references (43–45) and Supplementary Materials. Cells were frozen at 5–10 × $10^6$ cells per vial and were shipped on dry ice to the University of York. Human ureter specimens were collected for research under NHS Research Ethics Committee approval Leeds (East) REC 99/095 for anonymous use of surplus tissue following renal transplant surgery. Normal human urothelial (NHU) cells were isolated for primary cell culture from surgical tissues as described previously (46). For our study, NHU cell culture was initiated by thawing a vial of cryopreserved cells into one T-75 flask. The cells were maintained in KSFM (Thermo Fisher) complete medium. Cultures in passage 4 were used for RIME assays. Human blood samples were obtained from the York Tissue Bank Biofluid service, University of York. Primary $CD4^+$ T lymphocytes were isolated by immunomagnetic negative selection using an EasySep Human $CD4^+$ T Cell Isolation Kit (17952, STEMCELL Technologies) and an EasySep Magnet (18000, STEMCELL Technologies). $CD4^+$ T cell cultures were initially seeded at 1 × $10^6$ cells/mL in the culture medium. The time in culture was restricted to a maximum of 7 days to prevent T cell differentiation. Subject to achieving the desired cell count, all non-immortalised normal cells in finite culture, as well as established cell lines, were treated with 100 nM dexamethasone for 1 hour before harvest. PDX samples were not treated exogenously; instead, they were reliant on endogenous glucocorticoids from the host mouse at the time of collection. Detailed cell culture methods are provided in Supplementary Materials.

## Rapid Immunoprecipitation Mass spectrometry of Endogenous proteins (RIME)

Our DIA-NN-enabled RIME (DIANNeR) protocol builds on the established RIME methods (27, 28, 47), with specific modifications tailored to enhance performance across normal cells in finite culture from multiple tissues alongside established cell lines. For each condition, a minimum of three biological replicates were required. For normal cells in finite culture, biological replicates were obtained from three independent donors; for established cell lines, biological replicates were defined as separate passages. For PDXs, we analysed one

technical replicate from independent PDX tumours to provide donor-level biological replication consistent with our approach for normal cells.

Adherent cell cultures (MCF7, KMBC2, MDA-MB-231, normal breast epithelial and NHU cells) were subjected to the protocol as follows, which is optimised for 15 cm plates. If higher cell counts are required, multiple plates can be processed in parallel and the lysates combined after sonication. For each plate, the medium was removed and cell culture washed with 20 ml ice cold PBS before fixation. For each 15 cm dish, adherent cells were treated with a 20 ml solution of 2 mM disuccinimidyl glutarate (DSG, sc-285455A, Santa Cruz Biotechnology) in PBS for 20 minutes at ambient temperature. Subsequently, the DSG solution was discarded, and the cells were further crosslinked for 10 minutes using a 1% formaldehyde solution (28908, Thermo) in PBS at ambient temperature. Quenching was achieved by incubating the cells with 0.125 M glycine for 5 minutes. Following these steps, the crosslinking solution was removed and cells were washed twice with cold PBS and then harvested using a cell scraper and ice-cold PBS supplemented with 1X cOmplete Protease Inhibitor Cocktail (11873580001, Sigma). Cells were collected into 1.5 mL Protein LoBind tubes (EP0030108094, Eppendorf) and centrifuged (6000 × *g*, 4°C) for 3 minutes to pellet the cells and the supernatant was removed. Cells were then frozen at -80°C or processed immediately as per the sonication step.

For suspension (Jurkat and normal $CD4^+$ T cells) culture, 16% formaldehyde was added directly to cultures to a final concentration of 1%. After crosslinking the cells for 10 minutes at ambient temperature, quenching was performed using 0.125M glycine for 5 minutes. Double crosslinking using 2 mM disuccinimidyl glutarate (DSG) in PBS for 20 minutes at ambient temperature did not alter the number of identified interactors (pilot data not shown) and was therefore omitted. Cells were pelleted by centrifugation (500 × *g,* 4°C) for 3 minutes, resuspended in ice-cold PBS supplemented with 1X cOmplete Protease Inhibitor Cocktail, and transferred to 1.5 mL Protein LoBind tubes. The cells were washed twice with PBS including protease inhibitor, supernatant removed, and either frozen at -80°C or processed immediately for sonication.

PDX tissue samples were cryosectioned at 30 µm using a Leica CM1950 Cryostat. Sections were crosslinked in suspension with 2 mM DSG for 25 minutes, followed by 1% formaldehyde for 20 minutes. Crosslinking was quenched with 0.25 M glycine, and samples were centrifuged (2500 × *g*) for 3 minutes. Pellets were washed twice with cold PBS and resuspended in 6 ml LB3 (27, 28, 47) (composed of 10 mM Tris-HCl, pH 8.0, 100 mM NaCl, 1 mM EDTA, 0.5 mM EGTA, 0.1% sodium deoxycholate, 0.5% N-lauroylsarcosine sodium in molecular biology grade water) buffer, then subjected to sonication for 12–20 cycles, 30 seconds on / 1 minute off using a Ultrasonic Processor CP 750 with CV33 Probe (Cole Parmer) at 4°C, cycle time was based on tumour size and processed alongside other samples post-sonication.

For sonication of non-PDX samples, PBS-washed cell pellets containing up to 20 million crosslinked cells were resuspended and incubated at 4°C in 1 mL of Lysis Buffer 1 (27, 28, 47)

(composed of 50 nM HEPES, pH 7.5, 140 mM NaCl, 1mM EDTA, 10% glycerol, 0.5% NP-40, 0.25% Triton X100 in molecular biology grade water) for 10 minutes, followed by incubation in 1 mL of Lysis Buffer 2 (27, 28, 47) (10 mM Tris-HCl, pH 8.0, 200 mM NaCl, 1 mM EDTA, 0.5 mM EGTA in molecular biology grade water) for 5 minutes in sequence. After each incubation step, samples were centrifuged (2000 × *g,* 4°C) for 5 minutes to collect the cell/nuclei pellets. These pellets were then resuspended in 300 µL of Lysis Buffer 3, transferred to a 1.5 ml Bioruptor Pico Microtubes (Diagenode) and subjected to sonication with cycles of 30 seconds on / 30 seconds off using a Bioruptor Pico (Diagenode) for 5–10 cycles depending on the cell type and instrument. After sonication, 30 µL of the lysate was diluted with an equal volume of 1 × Tris/Glycine/SDS buffer (1610732, Bio-Rad) in 1:1 ratio. To confirm effective shearing, 10 µL of lysate was subject to RNAse A (2 µL) (AM2271, Thermo) treatment at 37°C for 1 hour, followed by proteinase K (2 µL) (10005393, Invitrogen) digestion at 65°C for 1 hour. The enzymatic reactions were terminated by heating at 95°C for 5 minutes. The purified DNA fragments were then visualised using SYBR Safe DNA Gel Stain (S33102, Thermo) on 1% agarose (A20090, Melford) gel with 1X TEA buffer as the running medium for gel electrophoresis. DNA fragments were visualised on a 1% agarose gel (Melford, A20090) stained with SYBR Safe DNA Gel Stain (Thermo, S33102) using 1X TAE buffer as the running medium. Samples that demonstrated adequate shearing (300–500 bp) proceeded to the next steps; otherwise, sonication conditions were optimised by adjusting the number of cycles. Following confirmation of adequate shearing, cell lysates were supplemented with Triton X-100 (X100, Sigma) to a final concentration of 1%. Subsequently, lysates were centrifuged (16,800 × *g*, 4°C) for 10 minutes to eliminate debris. The remaining supernatant was combined with previously prepared antibody-conjugated Pierce Protein A/G Magnetic Beads (88802, Thermo) and incubated overnight at 4°C with constant agitation. Depending on cell yield and experimental requirements, lysate from multiple 15 cm plates was pooled prior to the addition of the antibody conjugated beads.

For each RIME assay, 5 µg of anti-NR3C1 antibody (HPA004248, Atlas) or control normal rabbit IgG (2729, Cell Signaling Technology) was employed. The bead-antibody conjugates were prepared by washing either 10 µL (< $10^7$ cells) or 50 µL (> $10^7$ cells or PDXs) of magnetic bead suspension three times with 1 mL of protein-free blocking buffer (37584, Thermo). The beads were then resuspended in 500 µL of the same buffer, and the appropriate antibody was introduced to the suspension. The mixture was incubated at ambient temperature for 1 hour or at 4°C overnight. To eliminate any non-specifically bound antibodies, the bead-antibody conjugates were washed 3 times with 1 mL of protein-free blocking buffer (37584, Thermo) before being combined with the cell lysates.

After the cell lysates were incubated overnight with bead-antibody conjugate at 4°C, the beads were subject to ten washes within a 4°C cold room with a washing buffer (composed of 50 mM HEPES pH 7.6, 1mM EDTA, 1% NP40, 0.5M lithium chloride, 0.7% sodium deoxycholate in molecular biology grade water). The beads were quickly rinsed twice with freshly prepared 100mM ammonium bicarbonate buffer, and stored and maintained at -80°C until mass spectrometry-based proteomics analysis. On the day of analysis, the RIME

samples underwent on-bead trypsin digestion to produce peptides, following an established protocol (27).

## Mass spectrometry analysis

DDA sample analysis for antibody validation was undertaken using Thermo Fisher Orbitrap Fusion. Following on-bead digestion, peptides were loaded on a 50 cm EasyNano C18 column, followed by a 60 minute sample acquisition. Additionally, for DIA/DDA comparison, DDA samples are also loaded onto a 8 cm Performance C18 column, followed by 14.4 minute acquisition (100 SPD EvoSep One gradient) using a Bruker timsTOF HT in both DIA and DDA mode. Full details of Orbitrap Fusion and timsTOF HT DDA acquisition provided in Supplementary Methods.

The resulting LC-MS data (acquired in either Thermo's proprietary RAW format or Bruker's proprietary .d format) was processed using either FragPipe (v23) (48) for DDA data or via DIA-NN (2.0) software, searching against a human-specific SwissProt database appended with sequences of common proteomic contaminants. An *in-silico* predicted spectral library was created with the DIA-NN software, which was then refined through iterative searches against the DIA datasets resulting from the samples. The search criteria were set to maintain a false discovery rate (FDR) of 1%. Protein-level quantification was extracted using the high-precision quant-UMS tool within DIA-NN (49). For matched DIA/DDA comparison, DIA-NN output was then further analysed using FragPipe-Analyst (42) with Limma to establish $\log_2$ fold changes (LFC) and p-value for specific interactors, with sample minimal imputation and p-values subjected to Hochberg and Benjamini Correction.

The NR3C/GR sequence coverage plots for the comparison of antibodies were generated by the Scaffold Proteome Software from Orbitrap Fusion DDA data.

For our multi-tissue analysis, DIA Sample acquisition order was randomised, using the RAND function in Microsoft Excel, to mitigate any potential bias resulting from time- or injection count-correlated performance changes. Peptides were loaded onto EvoTip Pure tips for nanoUPLC using an EvoSep One system. A pre-set 30 SPD gradient was used with a 15 cm EvoSep $C_{18}$ Performance column (15 cm × 150 µm, 1.5 µm).

The nanoUPLC system was interfaced to a timsTOF HT mass spectrometer (Bruker) with a CaptiveSpray ionisation source. Positive PASEF-DIA, nanoESI-MS and $MS^2$ spectra were acquired using Compass HyStar software (Bruker, version 6.2). Instrument source settings were: capillary voltage, 1,500 V; dry gas, 3 l/min; dry temperature; 180°C. Spectra were acquired between *m/z* 100-1,700. DIA windows were set to 25 Th width between *m/z* 400-1201 and a TIMS range of 1/K0 0.6-1.60 V.s/cm$^2$. Collision energy was interpolated between 20 eV at 0.5 V.s/cm$^2$ to 59 eV at 1.6 V.s/cm$^2$.

Resulting LC-MS Data analysis was undertaken as above for DIA, and culminated in the production of a .parquet output from DIA-NN, which we subsequently processed using custom KNIME workflows to yield a protein group-centric dataset with additional filtering to

protein (q < 0.01, minimum of 2 peptides). Protein group-centric data was then analysed using the FragPipe-Analyst software as described for the DIA/DDA comparison.

## Quantitative DIA-NN MS multi-tissue dataset analysis

The GR DIA-NN-enabled RIME .tsv output was processed using the publicly hosted FragPipe-Analyst pipeline (http://fragpipe-analyst.nesvilab.org/) into .RData form and then analysed using the FragPipeAnalystR package.

## GO, Reactome, and KEGG over-representation analysis

The lists of genes for DDA-RIME for over-representation analysis were pre-filtered for a minimum of 2-peptides per protein, 1% peptide FDR and a protein threshold of 1% before enrichment analysis. For DDA-RIME, specific interactions were derived from differential enrichment analysis comparing the GR IP group to the IgG control group within the GR DIA-NN-enabled RIME datasets (LFC > 1, *p*-adjust < 0.05). Overrepresentation analysis of multiple terms was performed against GO, Reactome and KEGG terms through the g:Profiler (https://biit.cs.ut.ee/gprofiler/gost) R package (50, 51). Overrepresentation of specific terms was performed using clusterProfiler (v4.12.6) (52) and the *enricher* function.

## Patient Derived Xenografts

All *in vivo* studies were carried out in accordance with the UK Home Office (Scientific Procedures) Act 1986 under project licence PPL40/3645 and as described by Simões *et al.* (53). HBCx34 PDX was established from a luminal B breast cancer sample as previously described by Cottu *et al.* (54). In summary, small fragments of PDX tumours were implanted subcutaneously into the flanks of 8–12-week-old female NSG (NOD scid gamma, NOD.Cg Prkdcscid Il2rgtm1Wjl/SzJ) mice. These preclinical models are estrogen-dependent, so animals were administered 8 µg/ml 17-beta estradiol (Sigma-Aldrich, #E2758) in drinking water at least 4 days prior to implantation until the end of the experiment.

# Results

## Establishing a high-quality antibody for GR analysis by DDA-RIME

We optimised our choice of antibody to ensure specific and sensitive GR interactome analysis. To activate the GR nuclear interactome without inducing long-term transcriptional programmes or cellular phenotypic alterations regulated by GR genomic signalling, the strategy adopted throughout the entire study was to treat cultures with 100 nM Dex for 1 hour prior to harvesting (55, 56). We evaluated three potential antibodies (Atlas, HPA004248; CST, 12041; Thermo, PA1-511A) raised against GR to determine the optimal IP efficiency. The GR DDA-RIME and DIA-RIME assays with candidate antibodies were undertaken in parallel following the DDA-RIME protocol established for 100 million MCF7 cells (27, 28, 47).

We assessed the performance of these antibodies by the percentage peptide coverage on GR protein (Uniprot accession P04150) resulting from DDA-MS (47, 57). The polyclonal GR antibody (HPA004248), which had been used by the Human Protein Atlas (58), resulted in the highest peptide coverage of the bait protein (38%) amongst the antibody candidates (**Figure 1B**). To quantify the antibody's effectiveness, we assessed its capacity to precipitate known GR interacting proteins with a protein threshold of 1% FDR. We curated a reference list of 787 GR interacting proteins identified via high-throughput MS-based assays from BioGRID and a set of 499 proteins with experimental evidence (score over 0.15) from the STRING database (59, 60). The HPA GR antibody was able to capture 13% (106 out of 787) and 20% (99 out of 499) of these respective reference datasets. Hypergeometric tests confirmed the significant recovery of known GR interacting proteins ($p = 6.07 \times 10^{-22}$ for BioGRID and $p = 4.75 \times 10^{-34}$ for STRING). Additionally, STRINGdb network analysis of protein-protein interactions identified significantly more known interactions between the detected GR interacting proteins than expected by chance (p-value < 0.001, **Figure S1**).

As BioGRID and STRING do not provide the subcellular localisation or functional annotation of GR interactors (59, 60), we conducted functional enrichment analysis of these known GR interacting proteins detected by the HPA GR antibody using gProfiler (51). We searched Gene Ontology (GO) terms (61), Reactome (62) and KEGG pathways (63) to confirm the proteins detected were relevant to the transcriptional GR complex. Our analysis revealed significant enrichment for nuclear proteins associated with chromatin and transcription. These annotations align with the known function of Dex-activated GR as a TF regulating the expression of GR target genes (1, 19), thereby providing confidence in the specificity for the HPA GR antibody in our RIME-based GR interactome analysis (**Figures 1C and S2**).

## DDA-RIME was able to capture the GR interactome from 10 million cultured MCF7 cells

A central challenge to IP-MS methods is the efficient enrichment and detection from low input materials due to the sensitivity of MS instruments (29, 64). Before adapting the RIME method to a DIA workflow, we determined the minimum starting material feasible for effective GR DDA-RIME interactome analysis from cell lines. With 10 million Dex-treated MCF7 cells, representing a 10-fold reduction in cell number from our previous RIME studies (65), we followed the standard RIME procedures with minor modification (27) and double crosslinking (28). Specifically, we reduced the amount of anti-GR antibody from 10 µg to 5 µg, used protein-free blocking buffer (Pierce), as we previously noted a large background of Bovine Serum Albumin (BSA), and substituted 50 µL Dynabeads (Invitrogen) with 10 µL of Protein A/G Magnetic Beads (Pierce) per IP reaction. Using this modified protocol, followed by DDA-based MS acquisition, we successfully detected known GR-interacting proteins: 23% (183 out of 787) from BioGRID (59) and 29% (144 out of 499) from STRING (60)), based on our two reference datasets. The significant recovery of known GR interacting proteins, validated by hypergeometric test ($p = 2.12 \times 10^{-41}$ for BioGRID and $p = 3.74 \times 10^{-44}$ for STRING), demonstrates our method's effectiveness at a starting input of 10 million cells. Functional annotation of the GR interactome under these conditions revealed significant

enrichment in transcriptional machinery and associated activities. These results are consistent with the known biology of the active GR both in terms of its nuclear localisation and its role in transcription regulation **(Figure S3).** By contrast, analysis of the DMSO-only, low input, DDA-RIME showed weaker enrichment for terms related to nuclear ($p_{Dex} = 1.6 \times 10^{-79}$ vs $p_{DMSO} = 6.4 \times 10^{-42}$) and chromatin localisation ($p_{Dex} = 12 \times 10^{-12}$ vs $p_{DMSO} = 5.3 \times 10^{-4}$) as indicated by larger *p*-values for these terms, along with a loss of enrichment for key terms related to nuclear receptor signalling, the SWI/SNF complex and chromatin remodelling. However, terms related to chaperone proteins and steroid hormone related heat shock proteins remained relatively unchanged **(Figures S4 and S5).**

Our analysis therefore demonstrates that the GR DDA-RIME workflow was able to detect the GR interactome with a substantially reduced cell number and only minimal modifications to the protocol when applied to cell lines. The use of reduced starting material was associated with a modest increased background signal, and we acknowledge that enrichment of relevant KEGG and Reactome terms (**Figures S2 and S3**) was somewhat diminished under low cell number conditions.

Moreover, the interactomes identified from our low input optimised GR DDA-RIME workflow exhibited greater overlap with that of our reported GR interaction partners in the BioGRID and STRING databases (183 of 787 BioGRID entries and 144 of 499 STRING entries compared with 106 of 787 and 99 of 499 for proteins detected using the unmodified DDA-RIME protocol). These results demonstrate that our optimised GR DDA-RIME protocol enables the recovery of biologically relevant interactome data even when working with limited cell numbers, such as those of normal cell cultures, where expansion to the cells required the unmodified RIME protocol may not be feasible.

# DIA-NN-enabled RIME (DIANNeR) provides a label-free quantitative alternative to DDA-RIME with increased sensitivity for the analysis of normal cells

The quantitative RIME pipeline, qPLEX-RIME, enables the analysis of multiplex samples using isobaric labelling, such as Tandem Mass Tag (TMT)-labelling (28). Incorporating TMT-based proteomics to RIME provides precise quantification; however, current TMT labelling reagents are limited to a maximum of 35 samples (66–69), with a significantly increased per-sample cost associated with increasing from 18- to 32-plex. Given the scale of our panel (57 experimental samples), this presents practical challenges in both accommodating the total number of samples and the costs associated with TMT labelling during method development. Further, the batch effects of TMT-plexed analysis constrain the precision of quantification and reproducibility, and require additional data processing efforts to enable multi-batch integration (70). Label-free quantification allows the analysis of an extensive number of samples without isobaric label incorporation, thereby reducing costs and simplifying the sample preparation (71). Motivated by a recent methodological study showing that label-free DIA achieves results comparable to TMT labelling in DDA mode (72),

we sought to explore this approach in the context of GR interactome profiling. We further leveraged the Bruker timsTOF platform, which offers ion mobility separation (IMS) and provides additional advantages over the previously reported use of DIA-RIME on the Orbitrap Exploris 480 (73). On this basis, we performed a comparative GR DIA- and DDA-RIME assay using normal isolated human $CD4^+$ T lymphocytes from three separate individuals. Our investigation, which involved parallel label-free quantitative analysis on three platforms (Fusion DDA, timsTOF DDA and timsTOF DIA), aimed to benchmark the performance of our DIA protocol against the established use of DDA-RIME samples and the DDA on the timsTOF platform. While DIA RIME has previously been reported for a single cell line (73), we believe this is the first report undertaking a quantitative comparison of DIA vs DDA-RIME methods and on normal cells. To maximise the use of limited normal samples, we subjected all materials to IP using the normal GR antibody (HPA004248) to capture GR interactomes, followed by a secondary round of IP against normal rabbit IgG as isotype control to account for non-specific binding and common contamination during IP-MS proteomics analysis (74). In this assay, the DIA acquisition mode identified a significantly greater number of proteins than the DDA mode (t-test, n = 3, $p < 0.05$), using a minimum of two peptides per protein and a 1% FDR threshold and 100 million cells (**Figure 2A**). This enhanced proteome coverage in DIA was further supported by downstream analysis using FragPipe-Analyst (42), which identified a 2-fold increase in the number of proteins significantly enriched over the IgG control in DIA datasets when compared to either of the DDA acquisitions (**Figure 2B**). GR itself was among the most abundant and significantly enriched proteins in the DIA-RIME dataset, consistent with our previous findings from GR DDA-RIME in MCF-7 cells. Comparative analysis across the three platforms revealed that over 20% of proteins were commonly identified by all methods, with 87% of all detected proteins recovered using our DIA based protocol **(Figure 2C)**. Notably, the DIA-RIME approach uniquely captured several established GR-interacting proteins annotated in the BioGRID and STRING databases including NCOA3, SMARCC1, HMGB1, and HDAC2 (59, 60) (**Figure 2D**). Functional enrichment analysis of DIA-specific proteins further aligned with known GR biology, supporting the biological relevance of the detected interactome **(Figure 2E)**. Together, these results highlight the sensitivity and specificity of the DIA-RIME workflow, which integrates the timsTOF platform with DIA-NN and FragPipe-Analyst for mapping GR interactomes in normal cells.

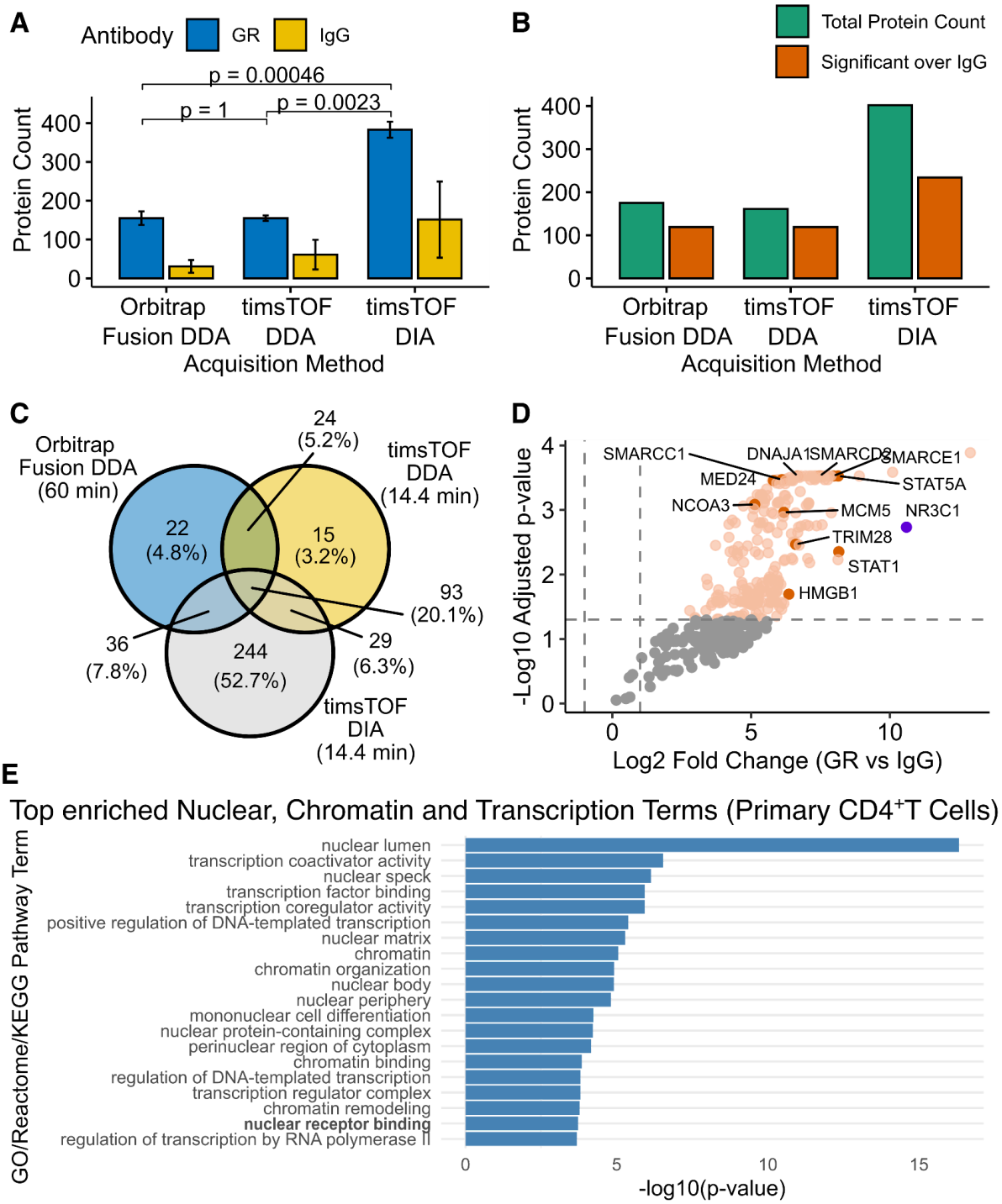


**Figure 2 DIA-RIME outperforms DDA in profiling GR interactomes from normal CD4⁺ T cells. (A)** Bar plot showing the number of proteins identified in GR-RIME samples by acquisition method. DIA identified significantly more proteins than either DDA approach (*t*-test, $n = 3$). **(B)** Comparison of the number of proteins identified before and after filtering for enrichment over IgG controls. **(C)** Venn diagram illustrating the overlap in proteomic coverage of GR interactomes across the three acquisition methods. **(D)** Volcano plot showing protein enrichment in GR-RIME samples relative to IgG controls using DIA-RIME. **(E)** Top 20 enriched nuclear, chromatin and transcription terms from analysis of GR interactors in CD4⁺T cells detected by DIA-RIME.

## Clustering by protein intensity of DIANNeR samples demonstrates tissue-specific differences in the GR interactome

In line with our aims, we applied DIANNeR to investigate the role of the GR interactome in differential tissue response. We analysed normal cells from three tissues **(Figure 3A)**, five matched cell lines, and three ER+ breast cancer PDX models. For each cell line, three biological replicates were generated from independent passages. In the case of normal cells, each biological replicate was obtained from a different donor. For the PDX models, material was derived from three distinct xenografts. For our analysis of normal human breast epithelial (44) and NHU (46, 75) cells, we performed three biological replicates; and for our normal $CD4^+$ T lymphocyte samples, we undertook four biological replicates. We conducted DIANNeR assays on all samples within our selected panel, adhering to our optimised GR IP protocols used for the DIA-MS experiment above, except in the case of PDX samples. As PDX samples were provided frozen, these were fixed and cryosectioned without thawing to preserve integrity and enable the permeability of crosslinking reagents, adapting the method established by Papachristou *et al.* (28). To minimise the effect of instrumental variations and accuracy, our first batch of DIANNeR samples were randomised and analysed concurrently using liquid chromatography (LC) followed by DIA-timsTOF MS (71, 76). We expanded our analysis after our initial sample acquisition to include MCF10A cells, the non-tumourigenic breast epithelial cell line, and the analysis of three ER+ PDX samples (BB3RC31, BB3RC29 and HBCx34 (53, 54)). To assess and, if necessary, control for potential batch effects, we prepared pooled GR and IgG DIANNeR samples for each cell type from our initial run. The pooled samples were then included in the subsequent MS analysis and randomised alongside the MCF10A and PDX samples. The resulting LC–MS spectral data from both batches were combined and searched using DIA-NN (v2.0). Minimal imputation was performed using KNIME, applying a 1% FDR cut-off, requiring a minimum of two peptides per protein, and filtering protein groups with $q < 0.01$. The resulting protein-centric dataset is hereafter referred to as the DIANNeR GR dataset (40), which identified a total of 7914 proteins across our panel of normal cells from primary tissues and cell lines.

Principal component analysis (PCA) of individual samples from DIANNeR GR dataset, using the FragPipeAnalystR pipeline, revealed that samples clustered primarily on the basis of our IgG control vs GR specific antibody when plotting PC1 and PC2 **(Figure 3B)**. GR-specific immunoprecipitations were clearly separated from IgG controls for all cellular models, demonstrating the specificity of GR interactome enrichment. Pooled samples from batch 2 clustered with their respective samples from batch 1, indicating minimal batch effects were observed after pre-processing. PDX samples were excluded from the PCA as they differed from other samples in treatment, processing, and composition, including mixed human and murine cells.

Interestingly, we also saw clustering by tissue of origin. GR interactomes for normal $CD4^+$ T cells and Jurkat cells formed a distinct clustering separate from epithelial-derived samples,

suggesting that Jurkat cells retain key features of the GR interactome observed in normal T cells. PCA clustering of cells of epithelial origin also demonstrated that the GR interactome from urothelium most closely resembled that of the bladder cancer cell line KMBC2.

To complement our PCA, we undertook hierarchical clustering of samples by protein intensity. Analysis of sample clustering within the DIANNeR GR dataset provided similar results to that seen by PCA, with the GR specific RIME pooled samples clustered with the samples from the initial batch of analysis. These results both provided confidence in the accuracy of reproducibility of the method and demonstrated the ability to expand datasets using pooled samples as controls for batch effects **(Figure 3C)**. As with PCA, Jurkat and normal $CD4^+$ T cells are clustered by tissue of origin for the GR specific pulldown, while the GR interactome for normal breast epithelium and urothelium is clustered together separately from established breast and bladder cancer cell lines. The GR interactome of the non-tumourigenic breast cell line MCF10A clustered most closely with the TNBC cell line MDA-MD-231.

Clustering for IgG control samples, as with the GR specific pulldowns, highlighted that $CD4^+$ T cell and Jurkat protein intensities clustered together. Unlike our GR interactome, the IgG control sample showed clustering of breast epithelial and urothelial cells separately along with related cell lines.

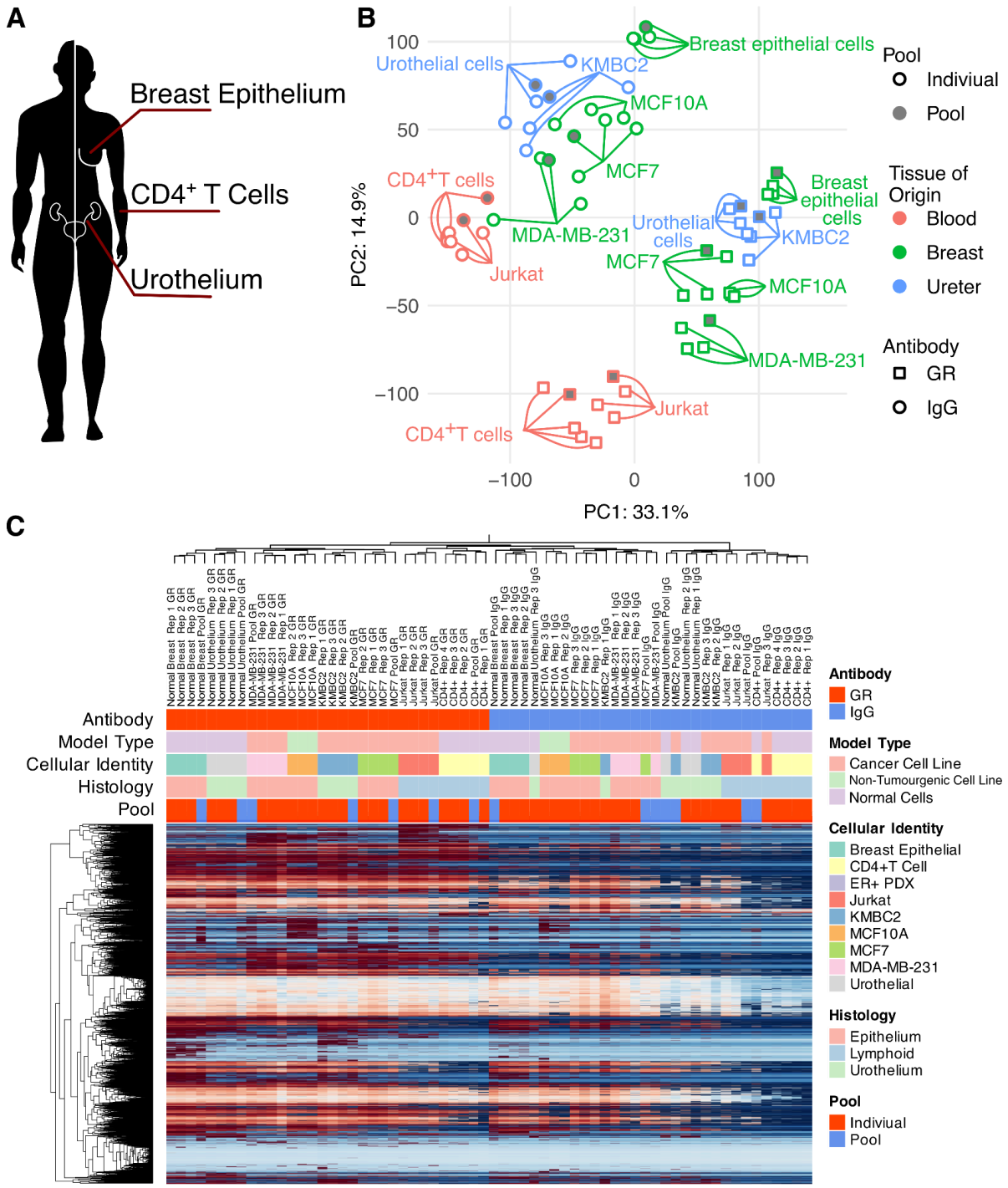


**Figure 3 Clustering of samples on detected protein intensity demonstrates reproducibility of DIA-NN enabled RIME (DIANNeR) for GR interactome analysis. (A)** Sites of primary tissue collection. **(B)** PCA analysis of protein intensities across all samples demonstrates clustering by antibody and tissue of origin for all cell-based IPs. **(C)** Hierarchical clustering of protein intensities for all samples from both batches clustered. GR RIME Pooled samples included in the second batch reproducibly clustered with their corresponding individual samples from the first batch. For GR specific pulldowns, clustering by epithelial vs lymphoid cell types dominates. The strength of IgG RIME samples clustering was primarily defined by tissue of origin rather than interactome.

## Differential analysis of GR interactomes across normal cells and cancer cell lines highlights tissue-specific GR interactions and functions

The differential selection and abundance of coregulators within the GR interactome across tissues are key factors in shaping the unique responses to glucocorticoids observed in different tissue types (2). We therefore undertook differential analysis of protein abundance in our samples using the FragPipe-Analyst pipeline to quantitatively identify GR specific interactions from our DIA data that were associated with tissue or model features. Fold enrichment of GR-interacting proteins was calculated for each protein in the GR IP group relative to the IgG control group using the linear model implemented in FragPipe-Analyst **(Results File S1)**. Undertaking hierarchical clustering, we generated the heat map of the LFC including all identified GR-interacting proteins that were significantly enriched (LFC > 2, and *p*-adjust < 0.01 in at least one model) **(Figure S7A)**. To aid interpretation of these results, we undertook PCA of the dataset to establish the top 25 contributing interactors from PC1, 2 and 3 **(Figure S7A-B)**. We used these interactors to highlight the most variable and informative GR interactions in a heatmap **(Figure 4A).** Additionally, we calculated the number of specific interactors **(Figure 4B)** for each model.

The PCA-prioritised GR interactome heatmap **(Figure 4A)** showed distinct differences in GR interacting proteins between model types. The heatmap and accompanying dendrogram revealed the following pattern: the two lymphoid models clustered separately from the other tissues; while MCF7 and the normal cells from the two epithelial tissues formed a second cluster. The final cluster was formed by the TNBC cell line, MDA-MB-231, and the non-tumourigenic breast epithelial cell line MCF10A cell line. KMBC2 was the only sample that displayed different clustering between the complete dataset **(Figures 4A and S7A)** and the prioritised heatmap, with the KMBC2 GR interactome clustering more closely to that of MDA-MB-231 and MCF10A, whereas in the full dataset, the KMBC2 data clustered separately. Overall, we interpreted that the prioritised GR interactors within **Figure 4A** were reflective and provide an informative overview of the model-specific GR interactomes.

Having determined a set of GR interactors that are reflective of the changes of GR-interacting proteins between tissues, we reviewed our list for proteins associated with key features of interest that aligned with known biology.

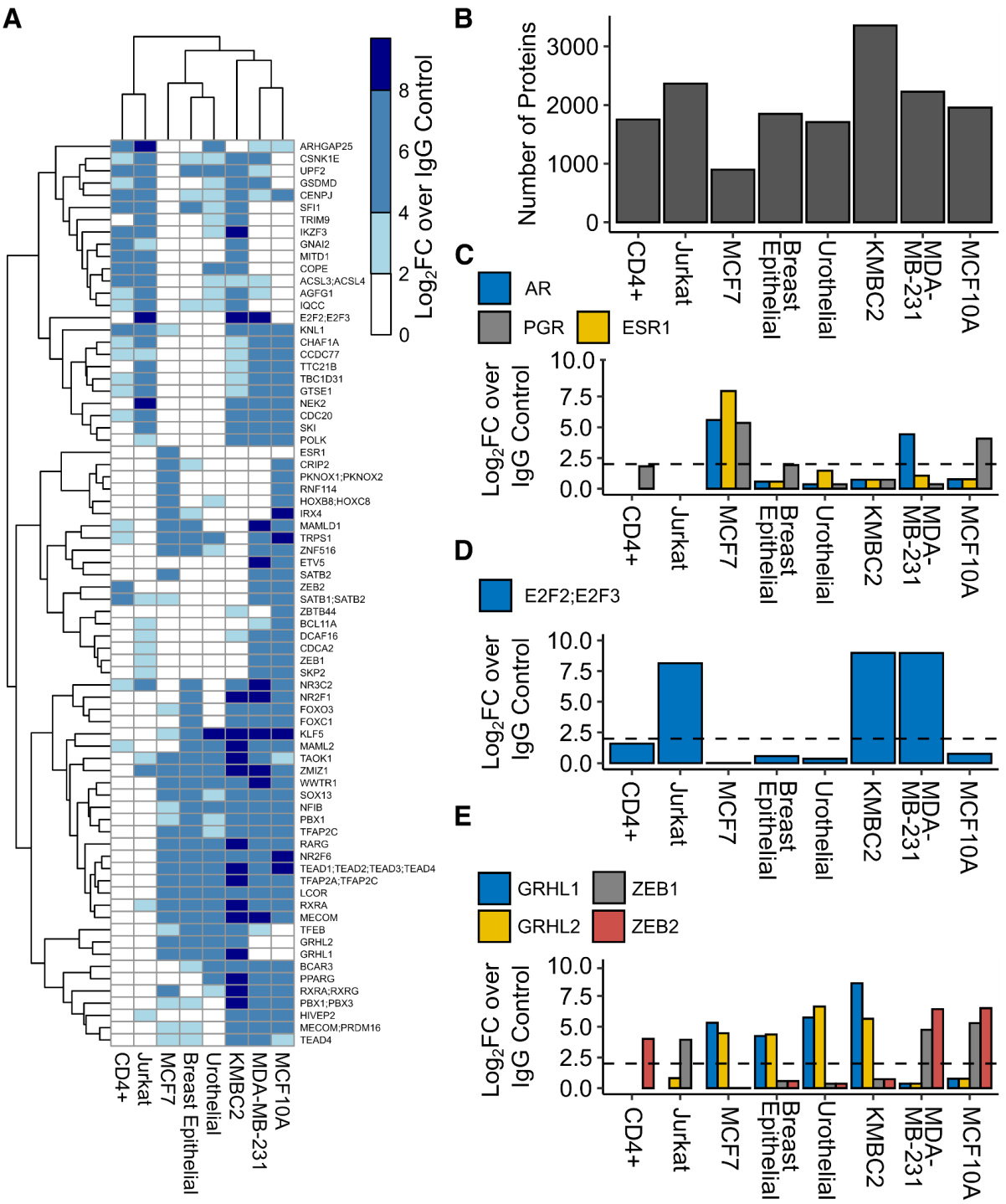


**Figure 4 GR interactor enrichment across cell types demonstrates context specific interactions. (A)** Heatmap showing the $\log_2$-fold change of selected transcription factors enriched over IgG control that drive hierarchical clustering of full data (Figure S7). **(B)** The number of unique proteins significantly enriched over IgG control for each model (LFC > 2 and *p*-adjust < 0.01). **(C)** Enrichment of sex steroid hormone receptors AR, PGR, and ESR1. ESR1 shows strong enrichment in MCF7 cells. **(D)** Enrichment of E2F2;E2F3 protein group across samples. All cancer cell lines, except MCF7, show an interaction of these proteins with GR. **(E)** Bar plots showing the enrichment of epithelial-associated GRHL1 and GRHL2 (blue/yellow), and epithelial-to-mesenchymal transition-associated ZEB1 and ZEB2 (grey/red). Dashed lines in bar plots indicate a LFC threshold of 2.

Of note, ERα (ESR1) was the only cofactor to be uniquely identified in one model (the MCF7 cell line). The ER+ cancer model specific ERα–GR interaction result reinforces findings within literature on the importance of GR regulation of ERα in ER+ breast cancers (13, 73, 77, 78). In such patients, activation of GR is associated with better outcome, whereas in TNBC patients, ERα is absent and GR-activating compounds increase metastatic risk. While not identified by our PCA, we additionally investigated the interaction of GR with the progesterone (PGR) and androgen (AR) receptors. AR was noted to specifically interact with GR in MCF7 and MDA-MB-231 cells, while PGR was noted to interact with GR in MCF10A and MCF7 cell lines.

The protein group E2F2;E2F3 was notable for a LFC > 8 in Jurkat, KMBC2 and MDA-MB-231 cell lines, but below our LFC < 2 cut-off for all other models. The only cancer cell line not to show a strong interaction between E2F2;E2F3 and GR was MCF7. Jurkat cells are considered resistant to GR mediated-apoptosis (79, 80), and our 1-hour Dex treatment captures early GR signalling prior to the onset of Dex-induced apoptosis in sensitive cells. During this phase, GR appears to engage with E2F TFs in a similar way to KMBC2 and MDA-MB-231 cell lines. Jurkat cells are highly proliferative with a reported doubling time of 26 hours (81), similar to that reported for MDA-MB-231 and KMBC (82, 83), and also lack the ERα–GR interaction of the MCF7 cell line.

Finally, we observed that GRHL1 and GRHL2 (TFs associated with epithelial identity and differentiation) interacted with GR in MCF7, normal breast epithelial and normal urothelial cells, and KMBC2 cells. By contrast, GR preferentially interacted with ZEB1 and ZEB2, key drivers of epithelial-to-mesenchymal transition (EMT) (84), in MDA-MB-231 cells, consistent with their mesenchymal phenotype (85). We also noted a GR interaction with ZEB1/2 in MCF10A cells, which was unexpected given their largely epithelial characteristics. This shift in GR interactions distinguishes MCF10A from normal breast epithelial cells and may reflect their immortalised status or subtle transitions in epithelial plasticity. In the normal $CD4^+$ T cells, only ZEB2 was detected in the GR interactome, while in Jurkat cells, only ZEB1 was observed. This pattern suggests that GR may engage with transcriptional regulators that reflect the underlying epithelial or mesenchymal state of each model. The selective association of GR with GRHL vs ZEB family proteins further supports a context-dependent role for GR in modulating cell phenotypes across different tissue types.

## Analysis of differential GR interactomes identifies tissue-specific features including an ERα-associated interactome in breast cancer cell lines

To investigate context-specific differences in the GR interactome across our breast models, we performed differential enrichment analysis between normal breast epithelial cells and two breast cancer cell lines, MDA-MB-231 and MCF7, and the non-tumourigenic cell line model MCF10A.

Differential binding analysis of MDA-MB-231 vs MCF7 GR interactomes **(Figure 5A)** revealed enhanced association of ZEB1 and ZEB2 with GR in the mesenchymal MDA-MB-231 line, consistent with our earlier PCA findings **(Figure 4E)**. Equally, we identified GRHL2 as one of the most significantly enriched GR interactors in the ER+ MCF7 cells, alongside significant enrichment of GRHL1.

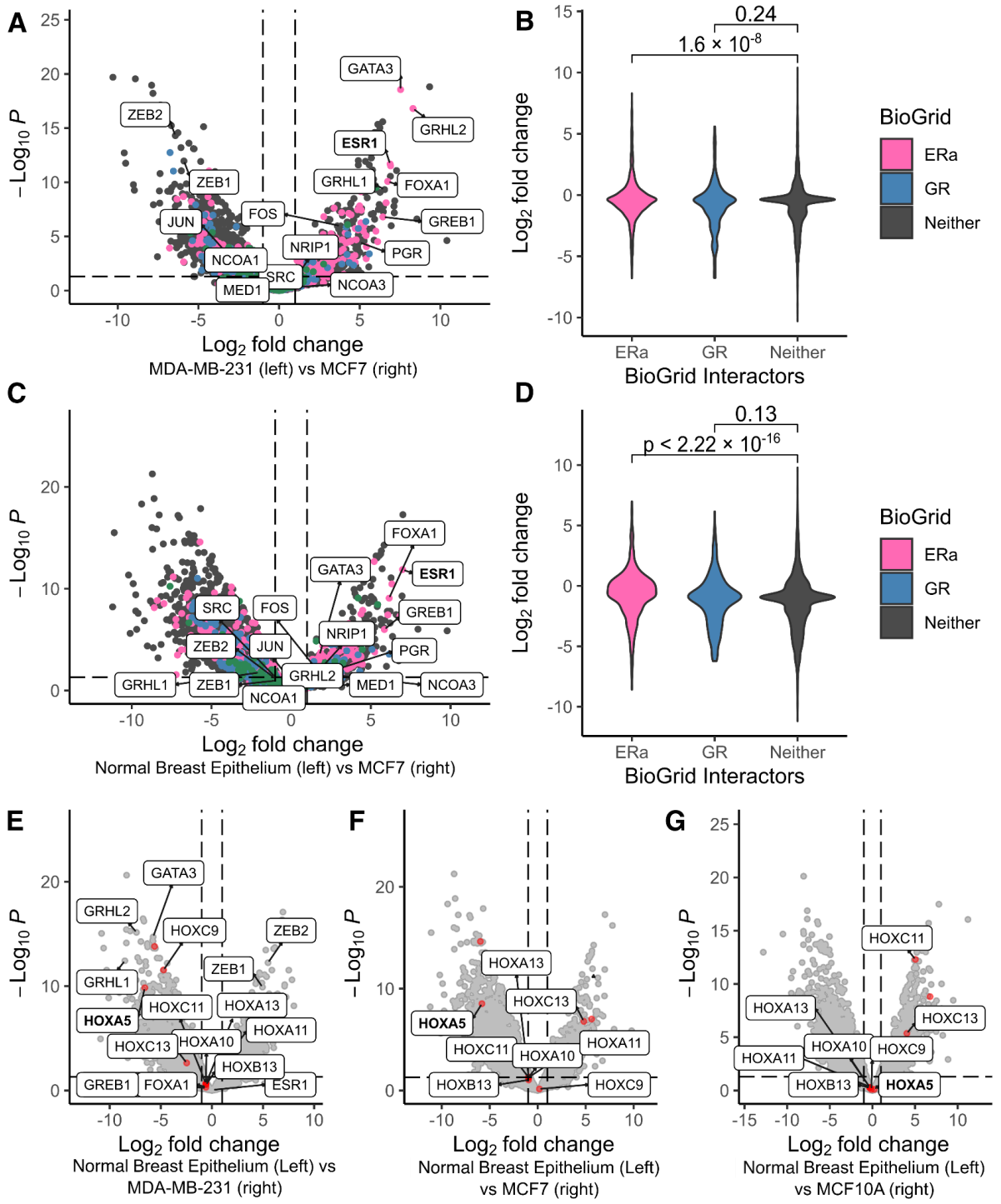


**Figure 5 DIANNeR identifies specific differences in the GR interactome between breast cancer cell lines and normal breast epithelial cells. (A)** Volcano plot comparing GR interactors in MCF7 and MDA-MB-231 cells, highlighting known ERα and GR-associated proteins. **(B)** Violin plot for LFCs for GR interactors from comparison

of MCF7 and MDA-MB-231 cell lines, stratified by their assignment as GR or ERα protein interactors as established from BioGrid. **(C)** Volcano plot comparison of the GR interactors in MCF7 cells and normal breast epithelium, highlighting known ERα and GR interacting proteins. **(D)** Violin plot for LFCs for GR interactors from comparison of MCF7 and normal breast epithelium cells and their assignment as GR or ERα protein interactors as established from BioGrid. **(E)** Volcano plot comparing GR interactors in MDA-MB-231 and normal breast epithelial cells, highlighting core ERα-associated proteins and HOX protein interactions. **(F)** Volcano plot comparing GR interactors in MCF7 and normal breast epithelial cells, highlighting HOX protein interactions. **(G)** Volcano plot comparing GR interactors in MCF10A cells and normal breast epithelial cells, highlighting HOX protein interactions. An interactive visualisation of these, and all following, results are available via a Shiny app at https://holding-lab.shinyapps.io/GR-volcano-plot.

Importantly, our DIANNeR pipeline recapitulated previous findings that GR and ERα interact in MCF7 cells (73). To assess this relationship, we analysed LFCs for ERα-interacting proteins as annotated in BioGRID. We observed a significant increase in LFCs of ERα-associated proteins in the MCF7 GR interactome relative to the MDA-MB-231 interactome, when compared to proteins not classified as GR or ERα interactors. No significant differences were observed in LFC between MCF7 and MDA-MB-231 for GR interacting proteins **(Figure 5B)**.

Comparison of the GR interactome in MCF7 cells to normal breast epithelial cells showed a similar enrichment for ERα and related proteins including FOXA1, GATA3, and GREB1 **(Figure 5C)**. We also detected a significant increase in LFCs of ERα-interacting proteins in MCF7 compared to normal breast epithelial cells **(Figure 5D)**. In contrast to our ER+ vs TNBC comparison, we saw no relative enrichment for the GRs interaction with either ZEB1, ZEB2, GRHL1, or GRHL2. In combination with the results shown in **Figure 4E**, these results suggest that the GRHL1 and GRHL2 interactions with GR are conserved between normal breast and ERα-positive MCF7 cells.

To explore further changes in GR-associated networks across different breast models, we compared the GR interactome in MDA-MB-231 cells with that of normal breast epithelial cells. Consistent with our PCA results, GR in MDA-MB-231 cells showed stronger associations with the mesenchymal transcription factors ZEB1 and ZEB2, whereas normal breast epithelial cells exhibited enhanced interactions with the epithelial regulators GRHL1 and GRHL2. We did not observe enrichment of ERα in normal cell samples, likely reflecting the low abundance of ER-positive cells within breast reduction specimens. However, we did detect enrichment of GATA3, a pioneer factor for ERα and a key marker of breast epithelial identity (86) **(Figure 5E)**.

In investigating differential GR interactions between normal tissues and cell line models, we identified tissue-dependent associations with HOX proteins. Notably, HOXA5 proteins were consistently enriched in the GR interactome of normal breast cells compared to both cancerous cell lines **(Figure 5E–F).** By contrast, no significant difference in HOXA5–GR interaction was observed when comparing normal cells with the non-tumourigenic MCF10A cell line **(Figure 5G)**; suggesting this interaction was preserved in both normal and immortalised epithelial contexts, and specifically lost during malignant transformation. This is notable given prior evidence that HOXA5 supports epithelial identity and suppresses

tumour progression in breast tissue, and loss of HOXA5 is associated with an acquisition of aggressive phenotypes (87).

## Distinct GR interactomes in epithelial and lymphoid contexts reveal Treg specific associations and an epithelial enrichment of SMARCD3

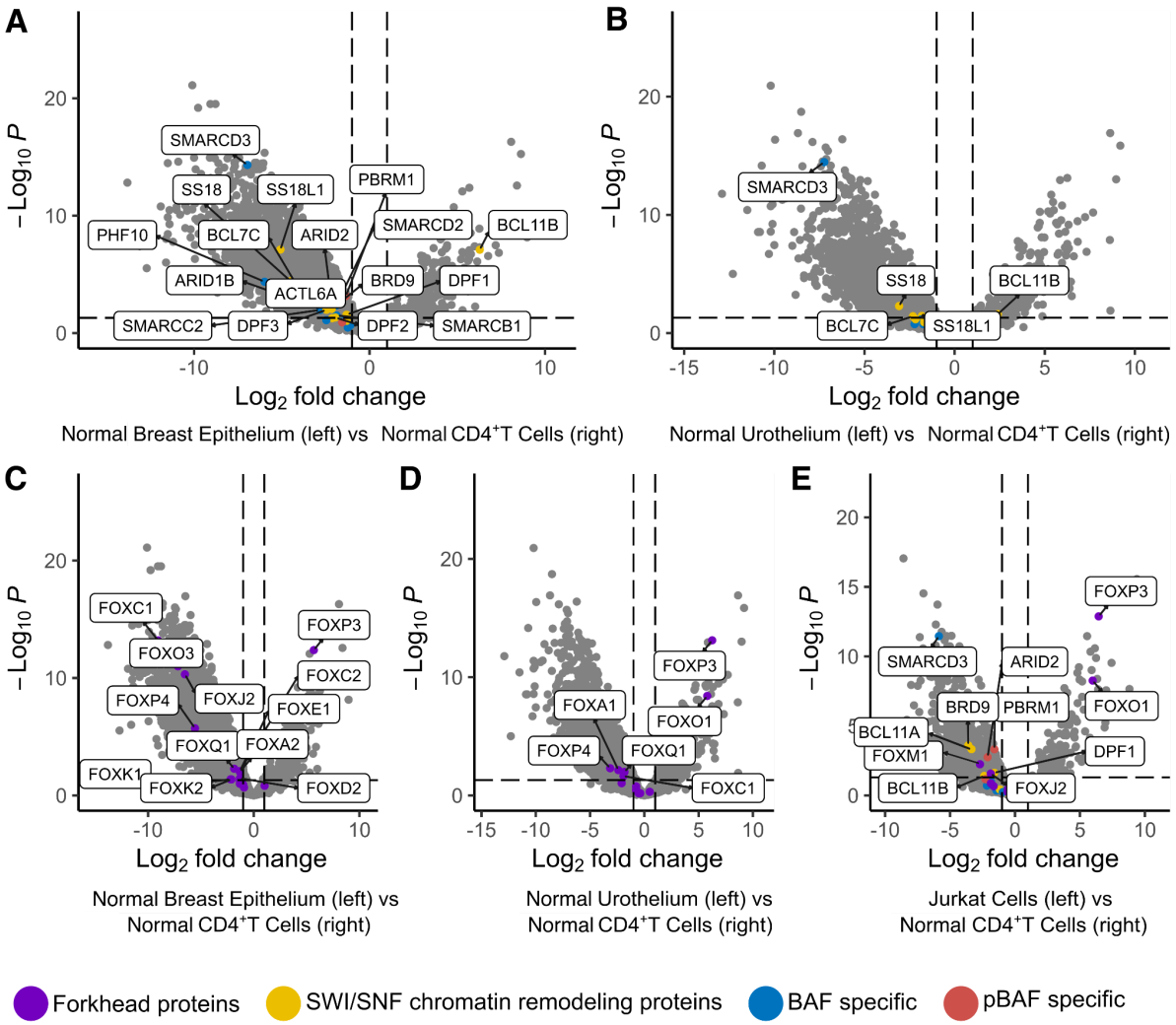


**Figure 6 SMARCD3 is significantly enriched in the epithelial GR interactome, and $T_{reg}$ specific protein FOXP3 is enriched in healthy CD4⁺ T cell GR interactome but lost in Jurkat cells. (A)** Volcano plot comparing GR interactors in normal breast epithelium and CD4⁺ T cells, highlighting proteins from the SWI/SNF complex with LFC > 2 and *p*-adjust < 0.05. **(B)** Volcano plot comparing GR interactors in normal urothelium and CD4⁺ T cells, highlighting SWI/SNF complex with LFC > 2 and *p*-adjust < 0.05. **(C)** Volcano plot comparing GR interactors in normal breast epithelium and CD4⁺ T cells, highlighting forkhead proteins. **(D)** Volcano plot comparing GR interactors in normal urothelium and CD4⁺ T cells, highlighting forkhead proteins. **(E)** Volcano plot comparing GR interactors in the Jurkat cell line and normal CD4⁺ T cells, highlighting forkhead proteins.

Given the previous results showing enrichment of the SWI/SNF complex in CD4⁺ T cells **(Figure S6)** and the well-established role of SWI/SNF in mediating GR-driven transcriptional responses (88–90), we next examined how SWI/SNF–GR interactions vary across tissue

types. In both the breast epithelium **(Figure 6A)** and urothelium **(Figure 6B)**, we observed significant differences in GR interactions with SWI/SNF members. While fewer significant differences to $CD4^+$ T cells were observed for the urothelium compared to the breast epithelium, both showed significant enrichment for the BAF-specific component SMARCD3. Notably, *SMARCD3* expression has previously been associated with improved prognosis in ER+ breast cancer (91), whereas our own analysis of TNBC patients (ER -ve by IHC, HER2 -ve by array) revealed the opposite association; higher *SMARCD3* expression correlation with worse outcome ($p$ = 0.0329, n=867, **Figure S8**) (92, 93). These contrasting trends align with the divergent effects of glucocorticoid signalling across breast cancer subtypes.

In comparing GR interactomes between epithelial and lymphoid cells, we identified BCL11B as the most significantly enriched SWI/SNF-associated GR interactor in $CD4^+$ T cells. Given the reported interdependence of BCL11B and FOXP3 in regulatory T (Treg) cell function (94), we explored GR interactions with the broader forkhead (FOX) protein family. Our analysis revealed that the interactions of GR with these proteins in the breast epithelial cells **(Figure 6C)** and urothelial cells **(Figure 6C)** were mostly unconserved; however, in both cases, FOXP3 was significantly enriched in $CD4^+$ T cells over the epithelial cells. This finding likely reflects the presence of a Treg subpopulation within our $CD4^+$ T cell samples, in which FOXP3 is a lineage-defining factor. Interestingly, this FOXP3–GR interaction was absent in the Jurkat T cell line **(Figure 6E)**, suggesting loss of Treg-specific GR signalling features in this immortalised lymphoid model.

## PDX provide *in vivo* validation of HOXA5- and SMARCD3–GR associations in healthy tissue and ERα-associated interactome enrichment in ER+ cancer

To provide *in vivo* validation of our cancer cell line results, we compared the GR interactome in ER+ breast cancer PDX material with that of normal breast epithelial cells. We first undertook individual analysis to confirm successful enrichment of the GR complex in each model, as PDXs were processed from frozen tissue, rather than live cells. Analysis showed a distinct LFC for GR-DIANNeR for a population of proteins in all three PDX models, when compared to IgG (**Figure 7A)**.

To confirm the specificity of the DIANNeR pipeline for GR-associated proteins in each individual PDX, we applied a threshold filter of LFC > 2 and performed overrepresentation analysis for previously identified GR-relevant terms **(Figure S5)**. All three PDX samples showed significant enrichment of terms related to nuclear receptor binding (GO:0016922), nuclear receptor-mediated steroid hormone signalling (GO:0030518), signalling by nuclear receptors (R-HSA-9006931) and transcription coregulator activity (GO:0003712) **(Figure 7B)**. Based on these results, we concluded that GR complexes were successfully enriched in all three models, thereby justifying their inclusion in subsequent combined analysis.

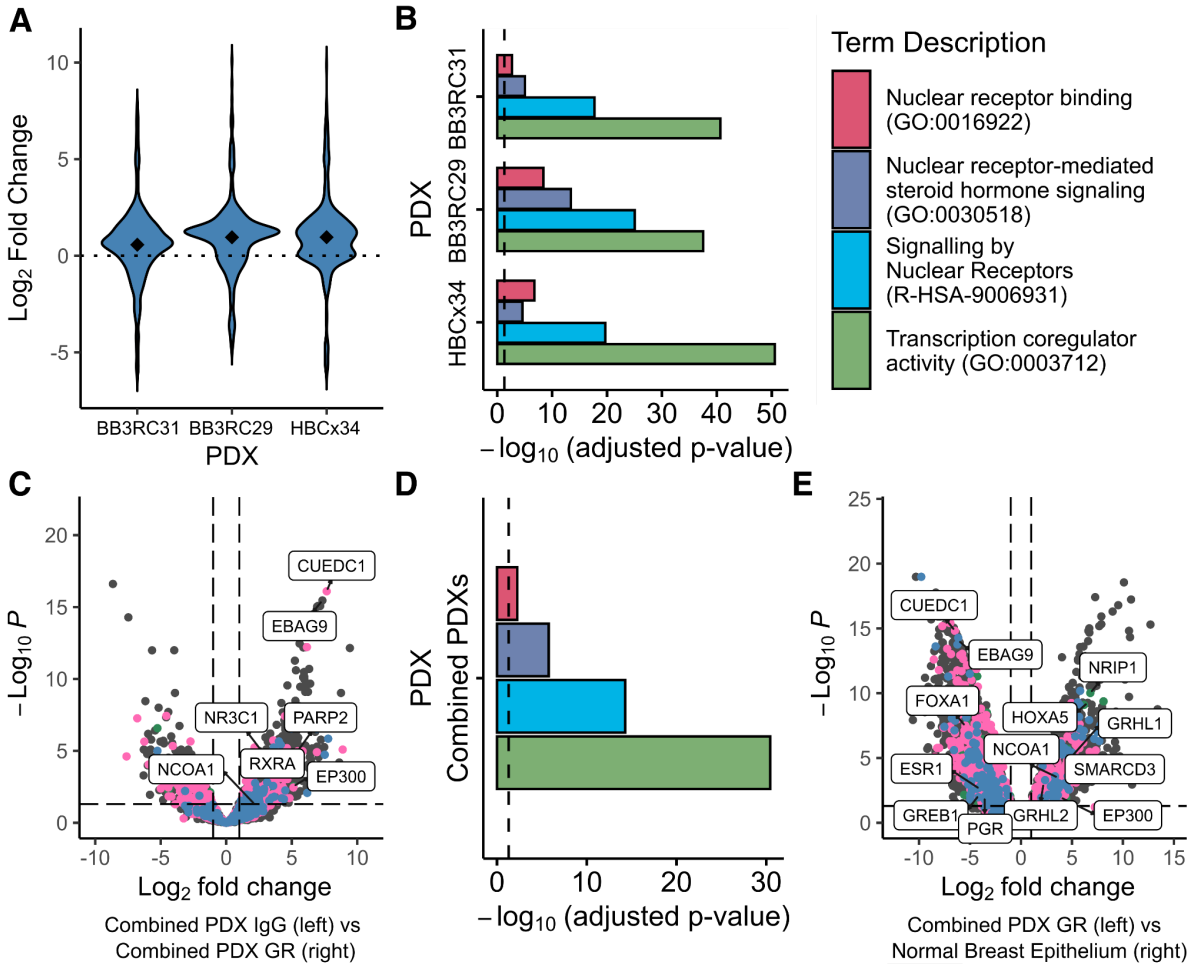


**Figure 7 ER+ PDXs show enrichment for the ERα complex compared to normal breast epithelium. (A)** Individual analysis of each PDX model revealed consistent enrichment of a subset of proteins in GR immunoprecipitates relative to IgG control. **(B)** Filtering proteins using LFC > 2 demonstrated significant enrichment for key terms related to the GR interactome. **(C)** Volcano plot of the combined GR-IP data from all three PDX models, showing significant enrichment of GR (NR3C1) along with known GR-associated proteins including EP300, NCOA1 and RXRA. Known GR interactors are coloured blue, known ERα interactors are pink. **(D)** Filtering proteins using LFC > 2 and *p*-adjust < 0.01 demonstrated significant enrichment for key terms related to the GR interactome. **(E)** Volcano plot comparing GR interactomes from the PDX models and normal breast epithelial cells. Known GR and ERα interactors are coloured as in (C).

Combining all three PDX models as biological replicates in FragPipe-Analyst, we confirmed enrichment of GR (NR3C1) along with several canonical GR interactors, including EP300, RXRA, and NCOA1 **(Figure 7C)**. Additionally, among the most significantly enriched proteins were CUEDC1 and EBAG9, both of which are ERα-associated interactors as reported by BioGRID. Filtering the combined samples on both LFC and significance (LFC > 2, *p*-adjust < 0.01), we observed pathway enrichment consistent with our individual PDX analyses **(Figure 7D)**.

Comparison of the GR interactome from PDX models with that of normal breast epithelium recapitulated our findings from cell lines. Specifically, we identified significant enrichment of ERα-associated proteins including ERα (*p*-adjust = 0.0015), GREB1 (*p*-adjust = 0.0075) and FOXA1 (*p*-adjust = $3.6 \times 10^{-8}$) from the ER+ PDX samples. In contrast, HOXA5 was significantly enriched in normal epithelium (*p*-adjust = $5.5 \times 10^{-10}$), consistent with our results comparing the normal epithelium and cell lines **(Figure 7E)**. These data support a selective loss of the HOXA5–GR interaction during malignant transformation and the acquisition of an ERα-enriched GR complex in ER+ breast cancer.

Consistent with our observation of the epithelial-specific enrichment of SMARCD3 in breast and urothelial cells, the SWI/SNF complex member was significantly depleted in the $CD4^+$ T cell GR interactome compared to PDX models (*p*-adjust = 0.013), further supporting an epithelial role for SMARCD3 in GR signalling.

# Discussion

In this study, we introduce DIANNeR (DIA-NN enabled RIME) to provide a proteomic workflow that advances RIME with the inclusion of data-independent acquisition (DIA) mass spectrometry (95), ion mobility separation on the Bruker timsTOF platform, and DIA-NN-based data analysis (40). Building upon well-established RIME (27), qPLEX-RIME (28) and ChIP-MS methodologies (29), our pipeline, DIANNeR, offers a label-free approach that facilitates rapid, cost-effective quantitative analysis of samples with high sensitivity at 10 million input cells.

By eliminating the need for isobaric labelling (72), DIANNeR removes associated reagent costs and provides scalable analysis of protein-protein interactions from low-input samples, while maintaining quantitative accuracy. To our knowledge, this is the first direct comparison of DIA and DDA acquisition modes performed on normal cells isolated from primary material. We demonstrate that DIANNeR identifies significantly more GR-associated proteins than conventional DDA methods, and does so with reduced acquisition time **(Figure 2)**.

Application of DIANNeR provided new insights into the tissue-specific effects of glucocorticoids, steroids that are widely used in clinical settings but known to exhibit highly context-dependent outcomes (1–3, 96). Although GR is broadly expressed, our data define differential cofactors and context-specific interactome compositions as central to tissue- and disease-specific transcriptional responses to glucocorticoid signalling (1, 4, 20).

PCA analysis and clustering of GR-enriched proteins **(Figure 4A)** revealed distinct tissue-specific features of the GR interactome across diverse biological contexts. The interaction between GR and ERα observed in the ER+ MCF7 cell line is consistent with previously reported results (73, 97, 98); and we build on these results with our characterisation of this interaction in our ER+ PDX models highlights its physiological relevance and represents a novel finding not captured in earlier studies **(Figure 7E)**.

Furthermore, we identified that the interactions of EMT-associated TFs (ZEB1/2 and GRHL1/2) with GR were directed by the mesenchymal or epithelial state of the respective cell type. This novel finding aligns with known regulatory mechanisms, as GRHL2 represses ZEB1 expression, while ZEB1 suppresses GRHL2, forming a feedback loop that modulates EMT in breast cancer (99). GRHL2 has also been shown to interact with ERα (100–103), further supporting the involvement of steroid receptor signalling within this transcriptional network, suggesting GR is embedded within the EMT regulatory networks that control epithelial plasticity.

Among all GR interactors identified in our cross-tissue PCA, three proteins were the most consistently enriched: TAOK1, ZMIZ1 and RXRA. ZMIZ1, previously characterised as an androgen receptor coactivator (104), has also been reported to interact with ERα (65), while RXRA has been shown to enhance GR response in T cells (105). We also detected several other nuclear receptors among the GR-associated proteins, including the mineralocorticoid receptor (NR3C2), supporting a broader role of nuclear receptor cross-talk within the GR interactome and tissue-specific function. Of note, ZMIZ1–GR was not detected in CD4+ T cells. ZMIZ1 was initially described as an AR-specific coactivator in LNCaP and CV-1 cells, with no coactivation of GR, ERα, or PGR, (104). More recent work has shown that this specificity is context-dependent: in MCF7 cells, ZMIZ1 interacts with ERα at the promoter of *E2F2* to enhance estrogen-mediated expression of cell cycle genes (65). Jurkat samples demonstrate enrichment for the ZMIZ1–GR interaction but lack detectable AR–, ERα–, and PGR–GR interactions; suggesting the presence of an alternative mediator of ZMIZ1–GR interactions in lymphoid cells. We hypothesise that this mediator is likely absent or poorly expressed in primary $CD4^+$ T cells. Future studies are needed to define the molecular basis of this interaction and its relevance to $CD4^+$ T cell GR signalling.

In the context of normal breast cells, we have identified a novel GR interaction with HOXA5 in the breast epithelium, which is retained in the non-tumourigenic MCF10A cell line, but lost in cancerous cell lines and ER+ PDX models **(Figures 5E–G)**. To our knowledge, only one previous study has linked these two proteins in epithelial breast cells, reporting inverse expression changes of *NR3C1* and *HOXA5* during mesenchymal-to-epithelial transition in the KRAS-HMLE-SNAIL EMT model following GN-25 treatment (106). However, that study did not explore a mechanistic or physical interaction between GR and HOXA5. Our finding aligns with prior reports that HOXA5 promotes epithelial identity and suppresses tumour progression in breast cancer (87) and the frequent loss of HOXA5 expression in cancer supports the absence of the GR–HOXA5 interaction in our malignant samples. While RIME-based approaches do not distinguish between direct protein-protein interactions and co-occupancy on chromatin, the significant interaction that we have observed in epithelium highlights a potentially important regulatory relationship. Moreover, as prior evidence shows HOXA5 expression is retinoic acid-responsive (107) and retinoic acid plays an essential role in breast development (108), our results suggest that HOXA5–GR interactions might be modulated by developmental signals. Future work should therefore mechanistically

investigate whether retinoic acid signalling or GR activation direct the HOXA5–GR association and its impact on carcinogenesis.

Beyond HOXA5, our analysis identified additional context-specific GR interactions with potential functional significance. Notably, we identified a SMARCD3–GR interaction **(Figure 6)** in epithelial cells (both breast and urothelial) that was absent in healthy $CD4^+$ T cells, suggesting cell type-specific recruitment of SMARCD3 to the GR complex. Expression of *SMARCD3*, a BAF complex-specific subunit, has previously been associated with favourable prognosis in ER+ breast cancer (91) whereas our own analysis of TNBC cohorts indicates its high expression correlates with poorer outcomes **(Figure S8)**. This is consistent with the diverse roles of GR activation across breast cancer subtypes, and supports a potential functional relevance of the SMARCD3–GR interaction. Together, these data suggest that targeting SMARCD3 may offer a strategy to selectively modulate GR activity in a subtype-specific manner, potentially allowing attenuation of deleterious GR responses in TNBC while preserving glucocorticoid efficacy in inflammatory conditions.

In conclusion, the DIANNeR method has expanded our capabilities to analyse nuclear receptor and TF interactomes, offering significantly improved performance compared to established DDA-based pipelines, supporting larger numbers of samples, reduced input requirements, and shorter instrument time, without the need for TMT labelling. Applying DIANNeR to the GR interactome has enhanced our understanding of tissue-dependent differences in the GR interactome and revealed opportunities to develop new targeted therapies for TNBC tumours that may limit the detrimental side effects of glucocorticoid treatment (7).

# Supplementary Data

Supplementary data are available online.

# Data Availability

All proteomic mass spectrometry datasets and results files are deposited in ProteomeXchange (PXD066547) and available to download from MassIVE (MSV000098634) [doi:10.25345/C5707X199], and the processed data for GR interactome across tissues is in supplementary file **Results File S1,** and via shiny app as an interactive figure https://holding-lab.shinyapps.io/GR-volcano-plot/, 10.5281/zenodo.16762042. The R code for data analysis and figures is available from https://github.com/Holding-Lab/DIANNeR, doi:10.5281/zenodo.16762026.

# Ethical Approval

This research was approved by the Biology Ethics Committee (BEC), University of York (AH202111).

# Funding

This work was supported by BBSRC (grant numbers BB/V000071/1, BB/X018288/1, BB/X018296/1 & BB/X511213/1) to ANH. JS was supported by a BBSRC White Rose Studentship (BB/T007222/1) and TFG was supported by MRC Discovery Medicine North (DiMeN) Doctoral Training Partnership Studentship (MR/W006944/1). Purchase of the Bruker timsTOF HT mass spectrometer was supported by BBSRC (grant number BB/W019272/1).

# Conflict of Interest

The authors declare no conflict of interest.

# Acknowledgements

The authors would like to thank all the anonymous volunteers from the University of York for their blood donation and the Biofluid service phlebotomists. The NHU cell culture was supported by a programme grant to the Jack Birch Unit from York Against Cancer. Jurkat cells were a kind gift from Dr Dimitris Lagos Lab, University of York. The authors wish to acknowledge the role of the Breast Cancer Now Biobank in collecting and making available the samples used in the generation of this publication, and all the patients who donated the samples. The authors would like to thank the Bioscience Technology Facility, University of York for their support in mass spectrometry analysis and flow cytometry analysis. The York Centre of Excellence in Mass Spectrometry was created thanks to a major capital investment through Science City York, supported by Yorkshire Forward with funds from the Northern Way Initiative, and subsequent support from EPSRC (EP/K039660/1; EP/M028127/1). The Viking cluster, which is a high-performance compute facility provided by the University of York, was used during this project. We are grateful for computational support from the University of York, IT Services and the Research IT team.

# References


1. Sacta,M.A., Chinenov,Y. and Rogatsky,I. (2016) Glucocorticoid Signaling: An Update from a Genomic Perspective. *Annu. Rev. Physiol.*, **78**, 155–180.

2. Gross,K.L. and Cidlowski,J.A. (2008) Tissue-specific glucocorticoid action: a family affair. *Trends Endocrinol. Metab.*, **19**, 331–339.

3. Burris,T.P., Solt,L.A., Wang,Y., Crumbley,C., Banerjee,S., Griffett,K., Lundasen,T., Hughes,T. and Kojetin,D.J. (2013) Nuclear receptors and their selective pharmacologic modulators. *Pharmacol. Rev.*, **65**, 710–778.

4. Ramamoorthy,S. and Cidlowski,J.A. (2016) Corticosteroids: Mechanisms of Action in Health and Disease. *Rheum. Dis. Clin. North Am.*, **42**, 15–31, vii.

5. Taves,M.D. and Ashwell,J.D. (2021) Glucocorticoids in T cell development, differentiation and function. *Nat. Rev. Immunol.*, **21**, 233–243.

6. Feng,Z., Marti,A., Jehn,B., Altermatt,H.J., Chicaiza,G. and Jaggi,R. (1995) Glucocorticoid and progesterone inhibit involution and programmed cell death in the mouse mammary gland. *J. Cell Biol.*, **131**, 1095–1103.

7. Pofi,R., Caratti,G., Ray,D.W. and Tomlinson,J.W. (2023) Treating the Side Effects of Exogenous Glucocorticoids; Can We Separate the Good From the Bad? *Endocr. Rev.*, 10.1210/endrev/bnad016.

8. Borin,C., Pieters,T., Serafin,V. and Ntziachristos,P. (2023) Emerging Epigenetic and Posttranslational Mechanisms Controlling Resistance to Glucocorticoids in Acute Lymphoblastic Leukemia. *HemaSphere*, **7**, e916.

9. Hoelzer,D., Bassan,R., Dombret,H., Fielding,A., Ribera,J.M. and Buske,C. (2016) Acute lymphoblastic leukaemia in adult patients: ESMO Clinical Practice Guidelines for diagnosis, treatment and follow-up†. *Ann. Oncol.*, **27**, v69–v82.

10. Caratti,G., Matthews,L., Poolman,T., Kershaw,S., Baxter,M. and Ray,D. (2015) Glucocorticoid receptor function in health and disease. *Clin. Endocrinol.* , **83**, 441–448.

11. Hesketh,P.J., Kris,M.G., Basch,E., Bohlke,K., Barbour,S.Y., Clark-Snow,R.A., Danso,M.A., Dennis,K., Dupuis,L.L., Dusetzina,S.B., *et al.* (2020) Antiemetics: ASCO Guideline Update. *J. Clin. Oncol.*, **38**, 2782–2797.

12. Mayayo-Peralta,I., Zwart,W. and Prekovic,S. (2021) Duality of glucocorticoid action in cancer: tumor-suppressor or oncogene? *Endocr. Relat. Cancer*, **28**, R157–R171.

13. Tonsing-Carter,E., Hernandez,K.M., Kim,C.R., Harkless,R.V., Oh,A., Bowie,K.R., West-Szymanski,D.C., Betancourt-Ponce,M.A., Green,B.D., Lastra,R.R., *et al.* (2019) Glucocorticoid receptor modulation decreases ER-positive breast cancer cell proliferation and suppresses wild-type and mutant ER chromatin association. *Breast Cancer Res.*, **21**, 82.

14. Obradović,M.M.S., Hamelin,B., Manevski,N., Couto,J.P., Sethi,A., Coissieux,M.-M., Münst,S., Okamoto,R., Kohler,H., Schmidt,A., *et al.* (2019) Glucocorticoids promote breast cancer metastasis. *Nature*, **567**, 540–544.

15. Lara Malik,N., Julien,A., Ausra,S.-G., Julien,J., Thuy Ha,P., Elisabetta,M., Anne,S., Ivan,B., Bassam,B., Olivier,T., *et al.* (2023) PRMT5 triggers glucocorticoid-induced cell migration in triple-negative breast cancer. *Life Science Alliance*, **6**, e202302009.

16. Abduljabbar,R., Negm,O.H., Lai,C.-F., Jerjees,D.A., Al-Kaabi,M., Hamed,M.R., Tighe,P.J., Buluwela,L., Mukherjee,A., Green,A.R., *et al.* (2015) Clinical and biological significance of glucocorticoid receptor (GR) expression in breast cancer. *Breast Cancer Res. Treat.*, **150**, 335–346.

17. Yang,N., Ray,D.W. and Matthews,L.C. (2012) Current concepts in glucocorticoid resistance. *Steroids*, **77**, 1041–1049.

18. Vandevyver,S., Dejager,L. and Libert,C. (2012) On the Trail of the Glucocorticoid Receptor: Into the Nucleus and Back. *Traffic*, **13**, 364–374.

19. Vettorazzi,S., Nalbantoglu,D., Gebhardt,J.C.M. and Tuckermann,J. (2022) A guide to changing paradigms of glucocorticoid receptor function—a model system for genome regulation and physiology. *FEBS J.*, **289**, 5718–5743.

20. Weikum,E.R., Knuesel,M.T., Ortlund,E.A. and Yamamoto,K.R. (2017) Glucocorticoid receptor control of transcription: precision and plasticity via allostery. *Nat. Rev. Mol. Cell Biol.*, **18**, 159–174.

21. Lonard,D.M. and O'Malley,B.W. (2012) Nuclear receptor coregulators: modulators of pathology and therapeutic targets. *Nat. Rev. Endocrinol.*, **8**, 598–604.

22. Guertin,M.J. and Lis,J.T. (2013) Mechanisms by which transcription factors gain access to target sequence elements in chromatin. *Curr. Opin. Genet. Dev.*, **23**, 116–123.

23. Stallcup,M.R. and Poulard,C. (2020) Gene-Specific Actions of Transcriptional Coregulators Facilitate Physiological Plasticity: Evidence for a Physiological Coregulator Code. *Trends Biochem. Sci.*, **45**, 497–510.

24. Poulard,C., Bittencourt,D., Wu,D.-Y., Hu,Y., Gerke,D.S. and Stallcup,M.R. (2017) A post-translational modification switch controls coactivator function of histone methyltransferases G9a and GLP. *EMBO Rep.*, **18**, 1442–1459.

25. Poulard,C., Kim,H.N., Fang,M., Kruth,K., Gagnieux,C., Gerke,D.S., Bhojwani,D., Kim,Y.-M., Kampmann,M., Stallcup,M.R., *et al.* (2019) Relapse-associated AURKB blunts the glucocorticoid sensitivity of B cell acute lymphoblastic leukemia. *Proceedings of the National Academy of Sciences*, **116**, 3052–3061.

26. Chinenov,Y., Gupte,R., Dobrovolna,J., Flammer,J.R., Liu,B., Michelassi,F.E. and Rogatsky,I. (2012) Role of transcriptional coregulator GRIP1 in the anti-inflammatory actions of glucocorticoids. *Proceedings of the National Academy of Sciences*, **109**, 11776–11781.

27. Mohammed,H., Taylor,C., Brown,G.D., Papachristou,E.K., Carroll,J.S. and D'Santos,C.S. (2016) Rapid immunoprecipitation mass spectrometry of endogenous proteins (RIME) for analysis of chromatin complexes. *Nat. Protoc.*, **11**, 316–326.

28. Papachristou,E.K., Kishore,K., Holding,A.N., Harvey,K., Roumeliotis,T.I., Chilamakuri,C.S.R., Omarjee,S., Chia,K.M., Swarbrick,A., Lim,E., *et al.* (2018) A quantitative mass spectrometry-based approach to monitor the dynamics of endogenous chromatin-associated protein complexes. *Nat. Commun.*, **9**, 2311.

29. Wierer,M. and Mann,M. (2016) Proteomics to study DNA-bound and chromatin-associated gene regulatory complexes. *Hum. Mol. Genet.*, **25**, R106–R114.

30. Greulich,F., Wierer,M., Mechtidou,A., Gonzalez-Garcia,O. and Uhlenhaut,N.H. (2021) The glucocorticoid receptor recruits the COMPASS complex to regulate inflammatory transcription at macrophage enhancers. *Cell Rep.*, **34**, 108742.

31. Hemmer,M.C., Wierer,M., Schachtrup,K., Downes,M., Hübner,N., Evans,R.M. and Uhlenhaut,N.H. (2019) E47 modulates hepatic glucocorticoid action. *Nat. Commun.*, **10**, 306.

32. Quagliarini,F., Mir,A.A., Balazs,K., Wierer,M., Dyar,K.A., Jouffe,C., Makris,K., Hawe,J., Heinig,M., Filipp,F.V., *et al.* (2019) Cistromic Reprogramming of the Diurnal Glucocorticoid Hormone Response by High-Fat Diet. *Mol. Cell*, **76**, 531–545.e5.

33. Mayayo-Peralta,I., Gregoricchio,S., Schuurman,K., Yavuz,S., Zaalberg,A., Kojic,A., Abbott,N., Geverts,B., Beerthuijzen,S., Siefert,J., *et al.* (2023) PAXIP1 and STAG2 converge to maintain 3D genome architecture and facilitate promoter/enhancer contacts to enable stress hormone-dependent transcription. *Nucleic Acids Res.*, 10.1093/nar/gkad267.

34. Gillet,L.C., Navarro,P., Tate,S., Röst,H., Selevsek,N., Reiter,L., Bonner,R. and Aebersold,R. (2012) Targeted Data Extraction of the MS/MS Spectra Generated by Data-independent Acquisition: A New Concept for Consistent and Accurate Proteome Analysis*. *Mol. Cell. Proteomics*, **11**, O111.016717.

35. Barkovits,K., Pacharra,S., Pfeiffer,K., Steinbach,S., Eisenacher,M., Marcus,K. and Uszkoreit,J. (2020) Reproducibility, Specificity and Accuracy of Relative Quantification Using Spectral Library-based Data-independent Acquisition. *Mol. Cell. Proteomics*, **19**, 181–197.

36. Muntel,J., Gandhi,T., Verbeke,L., Bernhardt,O.M., Treiber,T., Bruderer,R. and Reiter,L. (2019) Surpassing 10 000 identified and quantified proteins in a single run by optimizing current LC-MS instrumentation and data analysis strategy. *Mol Omics*, **15**, 348–360.

37. Vitko,D., Chou,W.-F., Nouri Golmaei,S., Lee,J.-Y., Belthangady,C., Blume,J., Chan,J.K., Flores-Campuzano,G., Hu,Y., Liu,M., *et al.* (2024) timsTOF HT Improves Protein Identification and Quantitative Reproducibility for Deep Unbiased Plasma Protein Biomarker Discovery. *J. Proteome Res.*, **23**, 929–938.

38. Heil,L.R., Damoc,E., Arrey,T.N., Pashkova,A., Denisov,E., Petzoldt,J., Peterson,A.C., Hsu,C., Searle,B.C., Shulman,N., *et al.* (2023) Evaluating the Performance of the Astral Mass Analyzer for Quantitative Proteomics Using Data-Independent Acquisition. *J. Proteome Res.*, **22**, 3290–3300.

39. Chakraborty,A.B., Berger,S.J. and Gebler,J.C. (2007) Use of an integrated MS--multiplexed MS/MS data acquisition strategy for high-coverage peptide mapping studies. *Rapid Commun. Mass Spectrom.*, **21**, 730–744.

40. Demichev,V., Messner,C.B., Vernardis,S.I., Lilley,K.S. and Ralser,M. (2020) DIA-NN: neural networks and interference correction enable deep proteome coverage in high throughput. *Nat. Methods*, **17**, 41–44.

41. Bruderer,R., Bernhardt,O.M., Gandhi,T., Miladinović,S.M., Cheng,L.-Y., Messner,S., Ehrenberger,T., Zanotelli,V., Butscheid,Y., Escher,C., *et al.* (2015) Extending the limits of quantitative proteome profiling with data-independent acquisition and application to acetaminophen-treated three-dimensional liver microtissues. *Mol. Cell. Proteomics*, **14**, 1400–1410.

42. Hsiao,Y., Zhang,H., Li,G.X., Deng,Y., Yu,F., Valipour Kahrood,H., Steele,J.R., Schittenhelm,R.B. and Nesvizhskii,A.I. (2024) Analysis and visualization of quantitative proteomics data using FragPipe-Analyst. *J. Proteome Res.*, **23**, 4303–4315.

43. Gomm,J.J., Browne,P.J., Coope,R.C., Liu,Q.Y., Buluwela,L. and Coombes,R.C. (1995) Isolation of pure populations of epithelial and myoepithelial cells from the normal human mammary gland using immunomagnetic separation with Dynabeads. *Anal. Biochem.*, **226**, 91–99.

44. Carter,E.P., Gopsill,J.A., Gomm,J.J., Jones,J.L. and Grose,R.P. (2017) A 3D in vitro model of the human breast duct: a method to unravel myoepithelial-luminal interactions in the progression of breast cancer. *Breast Cancer Res.*, **19**, 50.

45. Saunderson,E.A., Stepper,P., Gomm,J.J., Hoa,L., Morgan,A., Allen,M.D., Jones,J.L., Gribben,J.G., Jurkowski,T.P. and Ficz,G. (2017) Hit-and-run epigenetic editing prevents senescence entry in primary breast cells from healthy donors. *Nat. Commun.*, **8**, 1450.

46. Southgate,J., Hutton,K.A., Thomas,D.F. and Trejdosiewicz,L.K. (1994) Normal human urothelial cells in vitro: proliferation and induction of stratification. *Lab. Invest.*, **71**, 583–594.

47. Glont,S.-E., Papachristou,E.K., Sawle,A., Holmes,K.A., Carroll,J.S. and Siersbaek,R. (2019) Identification of ChIP-seq and RIME grade antibodies for Estrogen Receptor alpha. *PLoS One*, **14**, e0215340.

48. Yu,F., Haynes,S.E., Teo,G.C., Avtonomov,D.M., Polasky,D.A. and Nesvizhskii,A.I. (2020) Fast quantitative analysis of timsTOF PASEF data with MSFragger and IonQuant. *Mol. Cell. Proteomics*, **19**, 1575–1585.

49. Kistner,F., Grossmann,J.L., Sinn,L.R. and Demichev,V. (2023) QuantUMS: uncertainty minimisation enables confident quantification in proteomics. *bioRxiv*, 10.1101/2023.06.20.545604.

50. Reimand,J., Isserlin,R., Voisin,V., Kucera,M., Tannus-Lopes,C., Rostamianfar,A., Wadi,L., Meyer,M., Wong,J., Xu,C., *et al.* (2019) Pathway enrichment analysis and visualization of omics data using g:Profiler, GSEA, Cytoscape and EnrichmentMap. *Nat. Protoc.*, **14**, 482–517.

51. Kolberg,L., Raudvere,U., Kuzmin,I., Adler,P., Vilo,J. and Peterson,H. (2023) g:Profiler—interoperable web service for functional enrichment analysis and gene identifier mapping (2023 update). *Nucleic Acids Res.*, **51**, W207–W212.

52. Xu,S., Hu,E., Cai,Y., Xie,Z., Luo,X., Zhan,L., Tang,W., Wang,Q., Liu,B., Wang,R., *et al.* (2024) Using clusterProfiler to characterize multiomics data. *Nat. Protoc.*, **19**, 3292–3320.

53. Simões,B.M., Santiago-Gómez,A., Chiodo,C., Moreira,T., Conole,D., Lovell,S., Alferez,D., Eyre,R., Spence,K., Sarmiento-Castro,A., *et al.* (2020) Targeting STAT3 signaling using stabilised sulforaphane (SFX-01) inhibits endocrine resistant stem-like cells in ER-positive breast cancer. *Oncogene*, **39**, 4896–4908.

54. Cottu,P., Bièche,I., Assayag,F., El Botty,R., Chateau-Joubert,S., Thuleau,A., Bagarre,T., Albaud,B., Rapinat,A., Gentien,D., *et al.* (2014) Acquired resistance to endocrine treatments is associated with tumor-specific molecular changes in patient-derived luminal breast cancer xenografts. *Clin. Cancer Res.*, **20**, 4314–4325.

55. van der Laan,S., de Kloet,E.R. and Meijer,O.C. (2009) Timing is critical for effective glucocorticoid receptor mediated repression of the cAMP-induced CRH gene. *PLoS One*, **4**, e4327.

56. Severinova,E., Alikunju,S., Deng,W., Dhawan,P., Sayed,N. and Sayed,D. (2019) Glucocorticoid Receptor-Binding and Transcriptome Signature in Cardiomyocytes. *J. Am. Heart Assoc.*, **8**, e011484.

57. Cracknell,T., Mannsverk,S., Nichols,A., Dowle,A. and Blanco,G. (2020) Proteomic resolution of IGFN1 complexes reveals a functional interaction with the actin nucleating protein COBL. *Exp. Cell Res.*, **395**, 112179.

58. Uhlén,M., Björling,E., Agaton,C., Szigyarto,C.A.-K., Amini,B., Andersen,E., Andersson,A.-C., Angelidou,P., Asplund,A., Asplund,C., *et al.* (2005) A human protein atlas for normal and cancer tissues based on antibody proteomics. *Mol. Cell. Proteomics*, **4**, 1920–1932.

59. Oughtred,R., Rust,J., Chang,C., Breitkreutz,B.-J., Stark,C., Willems,A., Boucher,L., Leung,G., Kolas,N., Zhang,F., *et al.* (2021) The BioGRID database: A comprehensive biomedical resource of curated protein, genetic, and chemical interactions. *Protein Sci.*, **30**, 187–200.

60. Szklarczyk,D., Kirsch,R., Koutrouli,M., Nastou,K., Mehryary,F., Hachilif,R., Gable,A.L., Fang,T., Doncheva,N.T., Pyysalo,S., *et al.* (2023) The STRING database in 2023: protein-protein association networks and functional enrichment analyses for any sequenced genome of interest. *Nucleic Acids Res.*, **51**, D638–D646.

61. Harris,M.A., Clark,J., Ireland,A., Lomax,J., Ashburner,M., Foulger,R., Eilbeck,K., Lewis,S., Marshall,B., Mungall,C., *et al.* (2004) The Gene Ontology (GO) database and informatics resource. *Nucleic Acids Res.*, **32**, D258–61.

62. Milacic,M., Beavers,D., Conley,P., Gong,C., Gillespie,M., Griss,J., Haw,R., Jassal,B., Matthews,L., May,B., *et al.* (2023) The Reactome Pathway Knowledgebase 2024. *Nucleic Acids Res.*, **52**, D672–D678.

63. Kanehisa,M., Sato,Y., Kawashima,M., Furumichi,M. and Tanabe,M. (2016) KEGG as a reference resource for gene and protein annotation. *Nucleic Acids Res.*, **44**, D457–D462.

64. Mund,A., Brunner,A.-D. and Mann,M. (2022) Unbiased spatial proteomics with single-cell resolution in tissues. *Mol. Cell*, **82**, 2335–2349.

65. Zhao,W., Rose,S.F., Blake,R., Godicelj,A., Cullen,A.E., Stenning,J., Beevors,L., Gehrung,M., Kumar,S., Kishore,K., *et al.* (2024) ZMIZ1 enhances ERα-dependent expression of E2F2 in breast cancer. *J. Mol. Endocrinol.*, **73**.

66. Li,J., Cai,Z., Bomgarden,R.D., Pike,I., Kuhn,K., Rogers,J.C., Roberts,T.M., Gygi,S.P. and Paulo,J.A. (2021) TMTpro-18plex: The Expanded and Complete Set of TMTpro Reagents for Sample Multiplexing. *J. Proteome Res.*, **20**, 2964–2972.

67. Karp,N.A., Huber,W., Sadowski,P.G., Charles,P.D., Hester,S.V. and Lilley,K.S. (2010) Addressing accuracy and precision issues in iTRAQ quantitation. *Mol. Cell. Proteomics*, **9**, 1885–1897.

68. Christoforou,A.L. and Lilley,K.S. (2012) Isobaric tagging approaches in quantitative proteomics: the ups and downs. *Anal. Bioanal. Chem.*, **404**, 1029–1037.

69. Zuniga,N.R., Frost,D.C., Kuhn,K., Shin,M., Whitehouse,R.L., Wei,T.-Y., He,Y., Dawson,S.L., Pike,I., Bomgarden,R.D., *et al.* (2024) Achieving a 35-plex tandem mass tag reagent set through deuterium incorporation. *J. Proteome Res.*, **23**, 5153–5165.

70. Brenes,A., Hukelmann,J., Bensaddek,D. and Lamond,A.I. (2019) Multibatch TMT Reveals False

Positives, Batch Effects and Missing Values*. *Mol. Cell. Proteomics*, **18**, 1967–1980.

71. Rozanova,S., Barkovits,K., Nikolov,M., Schmidt,C., Urlaub,H. and Marcus,K. (2021) Quantitative Mass Spectrometry-Based Proteomics: An Overview. In Marcus,K., Eisenacher,M., Sitek,B. (eds), *Quantitative Methods in Proteomics*. Springer US, New York, NY, pp. 85–116.

72. Muntel,J., Kirkpatrick,J., Bruderer,R., Huang,T., Vitek,O., Ori,A. and Reiter,L. (2019) Comparison of Protein Quantification in a Complex Background by DIA and TMT Workflows with Fixed Instrument Time. *J. Proteome Res.*, **18**, 1340–1351.

73. Prekovic,S., Chalkiadakis,T., Roest,M., Roden,D., Lutz,C., Schuurman,K., Opdam,M., Hoekman,L., Abbott,N., Tesselaar,T., *et al.* (2023) Luminal breast cancer identity is determined by loss of glucocorticoid receptor activity. *EMBO Mol. Med.*, **15**, e17737.

74. Geisberg,J.V. and Struhl,K. (2004) Quantitative sequential chromatin immunoprecipitation, a method for analyzing co-occupancy of proteins at genomic regions in vivo. *Nucleic Acids Res.*, **32**, e151.

75. Cross,W.R., Eardley,I., Leese,H.J. and Southgate,J. (2005) A biomimetic tissue from cultured normal human urothelial cells: analysis of physiological function. *American Journal of Physiology-Renal Physiology*, **289**, F459–F468.

76. Piehowski,P.D., Petyuk,V.A., Orton,D.J., Xie,F., Moore,R.J., Ramirez-Restrepo,M., Engel,A., Lieberman,A.P., Albin,R.L., Camp,D.G., *et al.* (2013) Sources of technical variability in quantitative LC-MS proteomics: human brain tissue sample analysis. *J. Proteome Res.*, **12**, 2128–2137.

77. Horwitz,K.B., Costlow,M.E. and McGuire,W.L. (1975) MCF-7; a human breast cancer cell line with estrogen, androgen, progesterone, and glucocorticoid receptors. *Steroids*, **26**, 785–795.

78. West,D.C., Pan,D., Tonsing-Carter,E.Y., Hernandez,K.M., Pierce,C.F., Styke,S.C., Bowie,K.R., Garcia,T.I., Kocherginsky,M. and Conzen,S.D. (2016) GR and ER Coactivation Alters the Expression of Differentiation Genes and Associates with Improved ER+ Breast Cancer Outcome. *Mol. Cancer Res.*, **14**, 707–719.

79. Helmberg,A., Auphan,N., Caelles,C. and Karin,M. (1995) Glucocorticoid-induced apoptosis of human leukemic cells is caused by the repressive function of the glucocorticoid receptor. *EMBO J.*, **14**, 452–460.

80. Riml,S., Schmidt,S., Ausserlechner,M.J., Geley,S. and Kofler,R. (2004) Glucocorticoid receptor heterozygosity combined with lack of receptor auto-induction causes glucocorticoid resistance in Jurkat acute lymphoblastic leukemia cells. *Cell Death Differ.*, **11 Suppl 1**, S65–72.

81. Beesley,A.H., Palmer,M.-L., Ford,J., Weller,R.E., Cummings,A.J., Freitas,J.R., Firth,M.J., Perera,K.U., de Klerk,N.H. and Kees,U.R. (2006) Authenticity and drug resistance in a panel of acute lymphoblastic leukaemia cell lines. *Br. J. Cancer*, **95**, 1537–1544.

82. Sweeney,K.J., Swarbrick,A., Sutherland,R.L. and Musgrove,E.A. (1998) Lack of relationship between CDK activity and G1 cyclin expression in breast cancer cells. *Oncogene*, **16**, 2865–2878.

83. Yano,H., Maruiwa,M., Iemura,A., Mizoguchi,A. and Kojiro,M. (1992) Establishment and characterization of a new human extrahepatic bile duct carcinoma cell line (KMBC). *Cancer*, **69**, 1664–1673.

84. Parfenyev,S.E., Daks,A.A., Shuvalov,O.Y., Fedorova,O.A., Pestov,N.B., Korneenko,T.V. and Barlev,N.A. (2025) Dualistic role of ZEB1 and ZEB2 in tumor progression. *Biol. Direct*, **20**, 32.

85. Lehmann,B.D., Bauer,J.A., Chen,X., Sanders,M.E., Chakravarthy,A.B., Shyr,Y. and Pietenpol,J.A. (2011) Identification of human triple-negative breast cancer subtypes and preclinical models for selection of targeted therapies. *J. Clin. Invest.*, **121**, 2750–2767.

86. Sandström,J., Bomanson,J., Pérez-Tenorio,G., Jönsson,C., Nordenskjöld,B., Fornander,T., Lindström,L.S. and Stål,O. (2024) GATA3 and markers of epithelial-mesenchymal transition predict long-term benefit from tamoxifen in ER-positive breast cancer. *NPJ Breast Cancer*, **10**, 78.

87. Teo,W.W., Merino,V.F., Cho,S., Korangath,P., Liang,X., Wu,R.-C., Neumann,N.M., Ewald,A.J. and Sukumar,S. (2016) HOXA5 determines cell fate transition and impedes tumor initiation and progression in breast cancer through regulation of E-cadherin and CD24. *Oncogene*, **35**, 5539–5551.

88. Fryer,C.J. and Archer,T.K. (1998) Chromatin remodelling by the glucocorticoid receptor requires the BRG1 complex. *Nature*, **393**, 88–91.

89. Hsiao,P.-W., Fryer,C.J., Trotter,K.W., Wang,W. and Archer,T.K. (2003) BAF60a mediates critical interactions between nuclear receptors and the BRG1 chromatin-remodeling complex for transactivation. *Mol. Cell. Biol.*, **23**, 6210–6220.

90. John,S., Sabo,P.J., Johnson,T.A., Sung,M.-H., Biddie,S.C., Lightman,S.L., Voss,T.C., Davis,S.R., Meltzer,P.S., Stamatoyannopoulos,J.A., *et al.* (2008) Interaction of the glucocorticoid receptor with the chromatin landscape. *Mol. Cell*, **29**, 611–624.

91. Tropée,R., de la Peña Avalos,B., Gough,M., Snell,C., Duijf,P.H.G. and Dray,E. (2021) The SWI/SNF subunit SMARCD3 regulates cell cycle progression and predicts survival outcome in ER+ breast cancer. *Breast Cancer Res. Treat.*, **185**, 601–614.

92. Győrffy,B. (2024) Integrated analysis of public datasets for the discovery and validation of survival-associated genes in solid tumors. *Innovation (Camb.)*, **5**, 100625.

93. Győrffy,B. (2024) Transcriptome-level discovery of survival-associated biomarkers and therapy targets in non-small-cell lung cancer. *Br. J. Pharmacol.*, **181**, 362–374.

94. Hasan,S.N., Sharma,A., Ghosh,S., Hong,S.-W., Roy-Chowdhuri,S., Im,S.-H., Kang,K. and Rudra,D. (2019) Bcl11b prevents catastrophic autoimmunity by controlling multiple aspects of a regulatory T cell gene expression program. *Sci. Adv.*, **5**, eaaw0706.

95. Krasny,L. and Huang,P.H. (2021) Data-independent acquisition mass spectrometry (DIA-MS) for proteomic applications in oncology. *Molecular Omics*, **17**, 29–42.

96. Viegas,L.R., Hoijman,E., Beato,M. and Pecci,A. (2008) Mechanisms involved in tissue-specific apopotosis regulated by glucocorticoids. *J. Steroid Biochem. Mol. Biol.*, **109**, 273–278.

97. Yang,F., Ma,Q., Liu,Z., Li,W., Tan,Y., Jin,C., Ma,W., Hu,Y., Shen,J., Ohgi,K.A., *et al.* (2017) Glucocorticoid receptor:MegaTrans switching mediates the repression of an ERα-regulated transcriptional program. *Mol. Cell*, **66**, 321–331.e6.

98. Miranda,T.B., Voss,T.C., Sung,M.-H., Baek,S., John,S., Hawkins,M., Grøntved,L., Schiltz,R.L. and Hager,G.L. (2013) Reprogramming the chromatin landscape: interplay of the estrogen and glucocorticoid receptors at the genomic level. *Cancer Res.*, **73**, 5130–5139.

99. Wu,H.-T., Zhong,H.-T., Li,G.-W., Shen,J.-X., Ye,Q.-Q., Zhang,M.-L. and Liu,J. (2020) Oncogenic functions of the EMT-related transcription factor ZEB1 in breast cancer. *J. Transl. Med.*, **18**, 51.

100. Holding,A.N., Giorgi,F.M., Donnelly,A., Cullen,A.E., Nagarajan,S., Selth,L.A. and Markowetz,F. (2019) VULCAN integrates ChIP-seq with patient-derived co-expression networks to identify GRHL2 as a key co-regulator of ERa at enhancers in breast cancer. *Genome Biol.*, **20**, 91.

101. Reese,R.M., Helzer,K.T., Allen,K.O., Zheng,C., Solodin,N. and Alarid,E.T. (2022) GRHL2 enhances phosphorylated estrogen receptor (ER) chromatin binding and regulates ER-mediated transcriptional activation and repression. *Mol. Cell. Biol.*, **42**, e0019122.

102. Helzer,K.T., Szatkowski Ozers,M., Meyer,M.B., Benkusky,N.A., Solodin,N., Reese,R.M., Warren,C.L., Pike,J.W. and Alarid,E.T. (2019) The phosphorylated estrogen receptor α (ER) cistrome identifies a subset of active enhancers enriched for direct ER-DNA binding and the transcription factor GRHL2. *Mol. Cell. Biol.*, **39**.

103. Reese,R., Helzer,K. and Alarid,E.T. (2021) The transcriptional function of GRHL2 in hormone-dependent breast cancers. *J. Endocr. Soc.*, **5**, A819–A819.

104. Sharma,M., Li,X., Wang,Y., Zarnegar,M., Huang,C.-Y., Palvimo,J.J., Lim,B. and Sun,Z. (2003) hZimp10 is an androgen receptor co-activator and forms a complex with SUMO-1 at replication foci. *EMBO J.*, **22**, 6101–6114.

105. Tóth,K., Sarang,Z., Scholtz,B., Brázda,P., Ghyselinck,N., Chambon,P., Fésüs,L. and Szondy,Z. (2011) Retinoids enhance glucocorticoid-induced apoptosis of T cells by facilitating glucocorticoid receptor-mediated transcription. *Cell Death Differ.*, **18**, 783–792.

106. Azmi,A.S., Bollig-Fischer,A., Bao,B., Park,B.-J., Lee,S.-H., Yong-Song,G., Dyson,G., Reddy,C.K., Sarkar,F.H. and Mohammad,R.M. (2013) Systems analysis reveals a transcriptional reversal of the mesenchymal phenotype induced by SNAIL-inhibitor GN-25. *BMC Syst. Biol.*, **7**, 85.

107. Chen,H., Zhang,H., Lee,J., Liang,X., Wu,X., Zhu,T., Lo,P.-K., Zhang,X. and Sukumar,S. (2007) HOXA5 acts directly downstream of retinoic acid receptor beta and contributes to retinoic acid-induced apoptosis and growth inhibition. *Cancer Res.*, **67**, 8007–8013.

108. Cho,K.-W., Kwon,H.-J., Shin,J.-O., Lee,J.-M., Cho,S.-W., Tickle,C. and Jung,H.-S. (2012) Retinoic acid signaling and the initiation of mammary gland development. *Dev. Biol.*, **365**, 259–266.